Alma Mater Studiorum – Università di Bologna

School of Science
Department of Physics and Astronomy
Master Degree Programme in Astrophysics and Cosmology

Dynamical models for the counter-rotating galaxy NGC 1366

Graduation Thesis

Presented by:
Giulia Summa

Supervisor:
Chiar.ma Prof.ssa
Silvia Pellegrini

Academic year 2024-2025

Graduation date IV

Abstract

Early-type galaxies hosting counter-rotating (CR) stellar and/or gaseous components offer key insights into galaxy assembly. About 30% of S0 galaxies display such CR structures. The S0 galaxy NGC 1366 was found via spectroscopic studies as hosting CR stellar components. However, spectroscopy alone provide only a partial understanding of the system's dynamics. In this context, dynamical modelling serves as a powerful and complementary tool to investigate the galaxy's internal structure and dynamics. The aim of this work is to compare models with the kinematic data, to constrain the number of stellar components, their mass and mass-to-light ratio, and then the relative contribution of the CR component.

The dynamical modelling is performed solving the Jeans equations for axisymmetric, stationary, and collisionless multi-component systems with the `JASMINE2` code. A set of two-component models is explored by varying the Satoh parameters governing the decomposition of azimuthal motions, the mass fractions regulating the relative weight of each component or the mass-to-light ratios accounting for the stellar population properties. The projected photometric and kinematic fields are generated through a dedicated post-processing pipeline, extended with modules designed to complete the model, implement the weighting scheme, convert dimensionless quantities into physical units, and produce the final observables.

The modelling reveals a lower limit on the bulge mass fraction ($R_b > 0.336$), imposed by constraints within the Satoh decomposition framework. The explored two-component models successfully reproduce the observed line-of-sight velocity profile, particularly in the inner (out to $R \approx R_{e,b}$) and the outer ($1 \div 2$ kpc) observed regions. None of the models though is able to reproduce the velocity dispersion profile, failing to replicate the observed off-centre peaks. The outcome suggests that a more complex dynamical configuration is required to fully account for the galaxy's kinematics.

Contents

List of Figures

List of Tables

Introduction

Early-Type Galaxies (ETGs), encompassing elliptical (E), lenticular (S0), and dwarf systems, occupy a central and crucial role in advancing the understanding of galaxy evolution. Constituting approximately 20–30% of nearby galaxies at redshift $z \simeq 0$, modern observations reveal a remarkable diversity in their internal structures and dynamics, often featuring kinematic peculiarities such as counter-rotating components. Their relatively simple stellar populations, coupled with the availability of robust dynamical and photometric models, position ETGs as ideal laboratories for studying their long-term build-up of stellar mass across cosmic time. To accurately derive their structural and dynamical properties is fundamental to reconstruct the physical processes that have shaped these galaxies from the early Universe to the present epoch. In this context, stellar counter-rotating (CR) galaxies represent a subclass of systems crucial for probing the intricacies of assembly and angular momentum acquisition history of ETGs. These systems, categorised as multi-spin galaxies, host large-scale stellar components that rotate in opposite directions. A particularly informative subset of CR systems is the class of 2σ galaxies, defined by the presence of two symmetric off-centre peaks in the velocity-dispersion map. This kinematic signature arises from the superposition, in projection, of two large-scale CR stellar discs of comparable luminosity. While stellar counter rotation is rather uncommon, representing approximately 1.7% of all ETGs observed in the MaNGA survey and around 3.1% of S0/S0a galaxies, it is notably prevalent among lenticular (S0) galaxies, with roughly 30% exhibiting CR gaseous or stellar structures. The existence of CR galaxies highlights the importance of external gas accretion and minor mergers in shaping galaxy kinematics. In S0 galaxies, the CR stellar disc generally contains a younger stellar population that is kinematically aligned with the ionised gas, reinforcing the view that these discs usually form from acquired external material. The substantial diversity observed, including a spatial bimodality (inner versus outer CR configurations), and a wide range of stellar metallicities, suggests that their formation mechanisms are diverse, driven by scenarios such as accretion from cosmic filaments, wet mergers with gas-rich satellites, and tidal gas exchange between neighbours.

This Master's thesis investigates the lenticular galaxy NGC 1366, a spindle-shaped S0 system located within the Fornax cluster. Previous spectroscopic analysis suggested the presence of a counter-rotating stellar component. The disc component, which is the more luminous structure, rotates in the opposite direction relative to the bulge and

is therefore defined as the counter-rotating component throughout this work. Furthermore, a subsequent analysis of the spectrum at two positions centred at $R = 1$ kpc and $R = 2$ kpc revealed two counter-rotating stellar components within the disc region, indicating an even more complex configuration. However, relying solely on spectroscopic observations can only provide a partial understanding of the system's intricate internal dynamics.

The methodology employed in this study is dynamical modelling, utilising an output of the numerical code `JASMINE2`. This code solves the Jeans equations for axisymmetric, stationary, and collisionless multi-component systems, generating the progenitor model of a family of two-component systems sharing the same structural parameters. The study then explores the family of models by varying the mass-to-light ratios Υ_{*i}, accounting for the stellar population properties, and the Satoh parameters k_i, governing the decomposition of the azimuthal motion, ultimately producing the projected kinematic fields. By comparing these predictions with observational data, this study aims to constrain key physical properties of NGC 1366, including the number of components producing the observed kinematic fields, their mass-to-light ratios Υ_{*i}, their mass fractions R_i and the total stellar mass of the system.

The structure of this thesis is as follows: Chap. 1 provides a background on ETGs and describes the counter-rotation phenomenon. Chap. 2 details the general properties, observational data, and previous analyses of NGC 1366. Chap. 3 describes the numerical implementation of the multicomponent modelling approach using the `JASMINE2` code. Chap. 4 presents the specific two-component models constructed for NGC 1366, including the parameter exploration tests and the final results.

Chapter 1

Early-type galaxies and the counter-rotation phenomenon

This chapter provides an overview of early-type galaxies (ETGs) and introduces the phenomenon of counter rotation. Sec. 1.1 presents the general properties of ETGs, summarising their main morphological, structural, and kinematical characteristics. The section describes how the classical view of ETGs has evolved thanks to modern observations, which reveal a remarkable diversity in their internal structures and dynamics. It further discusses the global light profiles of ETGs, tracing the transition from the empirical de Vaucouleurs law to the more general Sérsic parametrisation, and reviews the kinematical classification derived from integral-field spectroscopy surveys, which distinguishes between regular and non-regular rotators. Sec. 1.2 focuses on galaxies hosting counter-rotating components, describing the different types of counter rotation observed in gaseous and stellar discs and their main observational signatures. The section also summarises the statistical occurrence of such systems in large surveys and discusses the principal formation mechanisms proposed to explain their origins.

1.1 Early-type galaxies

Early-type galaxies, comprising elliptical (E), lenticular (S0), and dwarf systems, constitute one of the two principal morphological families of the Hubble sequence (Hubble 1936), located in the handle of the empirical tuning fork diagram.

In the Local Universe (i.e., at redshift $z \simeq 0$), ETGs account for approximately 20–30% of the observed nearby galaxies and are less numerous than late-type galaxies (LTGs), which occupy the right-hand side of the Hubble diagram and include spiral (S) and irregular (Irr) systems.

Prior to the 1980s, ETGs were commonly regarded as dynamically simple, rotationally flattened ellipsoids with smooth and featureless light distributions, no spiral arms, generally lacking significant interstellar gas and dust, and exhibiting red optical colours indicative of old, metal-rich, passively evolving stellar populations with minimal

ongoing star formation.

Although these general characteristics remain broadly valid, modern observations have shown that ETGs exhibit a wide structural and dynamical diversity:

- many ellipticals are not flattened by rotation but are intrinsically anisotropic systems;
- they host an interstellar medium (ISM) predominantly in the hot phase ($T > 10^6$ K), while in some cases cold ISM has been accreted from companion galaxies;
- low-mass ETGs frequently contain intermediate-age stellar populations;
- all harbor a central supermassive black hole (SMBH);
- a significant fraction of ETGs exhibit kinematic peculiarities, such as counter-rotating structures, reflecting a complex and often disturbed assembly history.

1.1.1 Global galaxy profiles

For several decades, elliptical galaxies were believed to be well represented by the de Vaucouleurs $R^{1/4}$ law (Vaucouleurs 1948), introduced to describe the projected luminosity density (or surface brightness) of ellipticals and of the spheroidal components of disc galaxies.

Subsequent studies and modern photometry demonstrated that this parametrisation does not adequately describe the full variety of observed light profiles: for a large fraction of ETGs the $R^{1/4}$ formula is only a first-order approximation. Michard (1985) noted that systematic deviations from the $R^{1/4}$ trend are similar for elliptical galaxies of similar luminosities and the results from Schombert (1986) and Binggeli et al. (1991) suggested a correlation between the shape of the light profile and the total luminosity of the galaxy. For bulges of S0s, Capaccioli (1987) noted that the minor axis light profiles of edge-on objects deviate systematically from the $R^{1/4}$ law.

Caon et al. (1993) showed that many ETGs are better fitted by the more general Sérsic model (Sérsic 1968), i.e. a power law in which the exponent is the free parameter $1/n$. Introducing a scale radius, the $R^{1/n}$ law is defined as

$$I(R) = I_e \exp\left\{-b_n\left[\left(\frac{R}{R_e}\right)^{1/n} - 1\right]\right\}, \tag{1.1}$$

where R_e is the effective radius, I_e is the surface brightness at R_e, and the parameter b_n, often referred to as the Sérsic constant, is a normalisation factor that depends on the Sérsic index n and is defined so as to ensure that the effective radius R_e encloses half of the total luminosity of the profile. The good correlation between n and the global parameters of the galaxy, such as total luminosity and effective radius R_e, leads to the approximated analytical expression for the Sérsic constant, given by $b_n \simeq 2n - 0.327$ for $0.5 < n < 10$ (Capaccioli 1989).

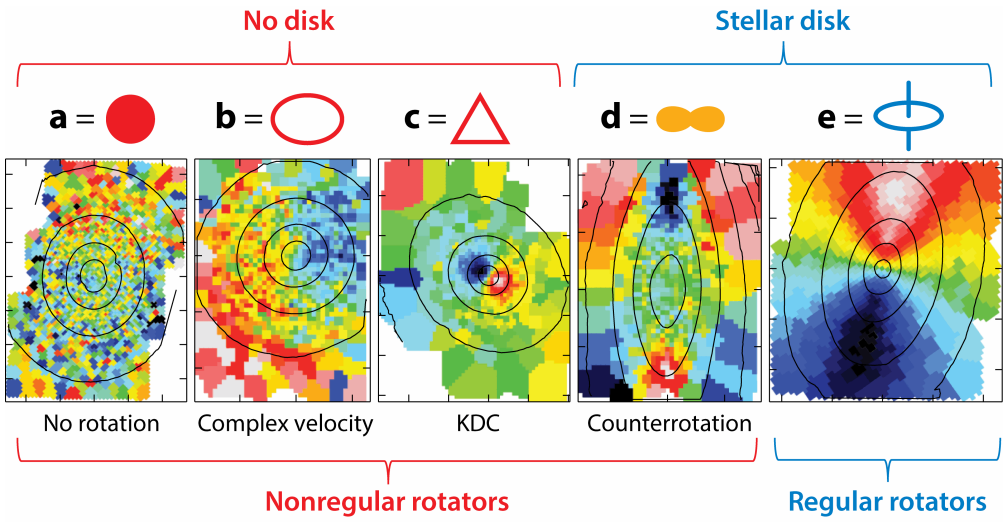

Figure 1.1: Scheme of the morphological classifications based on stellar kinematics. The kinematic features in large samples of ETGs can be qualitatively described by five classes: *(a)* no clearly detectable rotation, *(b)* clear but non-regular rotation, *(c)* kinematically distinct cores (KDCs), *(d)* counter-rotating discs, and *(e)* regular, extended, disc-like rotation. Taken from Cappellari (2016).

A key result of these studies is that the Sérsic index n, which quantifies the concentration of the light distribution (i.e. the ratio between the amount of light contained within the central regions and the amount in the outskirts), increases systematically with the total luminosity of the galaxy. This trend suggests that more luminous ellipticals have more centrally concentrated profiles (Cappellari 2016). The observed correlation has been interpreted as reflecting variations in the structural properties of elliptical galaxies with luminosity (Cappellari 2016). Nonetheless, part of the trend may also arise from systematic differences in the fraction of hidden discs within ETGs. It is likely that both effects contribute, since the Sérsic indices of spirals and S0 bulges generally differ from those of massive ellipticals (Kormendy et al. 2009).

1.1.2 Kinematical classification

The advent of integral-field spectroscopy (IFS) has profoundly revised the classical view of ETGs. Observations from surveys such as ATLAS^{3D}, a volume-limited sample of 260 nearby ETGs (Cappellari et al. 2011; Emsellem et al. 2011), have revealed a clear kinematic dichotomy between two distinct classes of objects: fast and slow rotators, also called regular (RR) and non-regular rotators (NRR) (Cappellari 2016). In the velocity maps, regular rotators exhibit a regular pattern of rotation projected along the line of sight; non-regular rotators, instead, are characterised by more complex structures (including cases where the rotation is not detectable).

The peculiar kinemetric features recognised by Krajnović et al. (2011), through a

Group	Features	Comment	#
a - no rotation (NRR)	NRR/LV	low-level velocity	7
b - complex velocity (NRR)	NRR/NF	no feature	12
c - KDC (NRR)	NRR/KDC	kinematically distinct core	11
	NRR/CRC	counter-rotating core	7
	RR/CRC	counter-rotating core	1
d - counter rotation (NRR)	NRR/2σ	double σ	7
	RR/2σ	double σ	4
e - simple rotation (RR)	RR/NF	no feature	171
	RR/2M	double maxima	36
	RR/KT	kinematic twist	2
f - unclassified (U)	U	unclassified	2

Table 1.1: Summary of kinematic groups and features in the ATLAS^{3D} sample, with a description of each feature and the number of galaxies identified. Adapted from Krajnović et al. (2011).

quantitative analysis of velocity maps using elliptical rings and Fourier expansion to characterise rotational structure and deviations from simple rotation, are the following:

no-feature (NF): velocity maps where the kinematic position angle (i.e. the orientation of the rotation axis, defined as the angle of the line connecting the maximum and minimum line-of-sight velocities) remains constant with radius;

double maxima (2M): velocity maps with a radial profile showing a rapid rise in rotational velocity, followed by a decline and a subsequent additional rise, indicating two local maxima in the rotation curve;

kinematic twist (KT): cases where the orientation of the galaxy's rotation axis changes smoothly across the velocity map, with a total variation of at least 10°;

kinematically distinct core (KDC): systems where there is an abrupt change in the kinematic position angle larger than 30° between adjacent regions, accompanied by a drop of the rotation velocity amplitude to zero in the transition zone;

counter-rotating core (CRC): a special case of the KDC, where the change in kinematic position angle is approximately 180°, indicating two components rotating in opposite directions;

low-level velocity (LV): maps characterised by very low stellar rotation amplitude at all radii;

double sigma (2σ): galaxies showing two symmetric peaks in the velocity-dispersion map, located on opposite sides of the centre along the major axis, consistent with the presence of two counter-rotating stellar discs overlapping in projection.

Accordingly to the peculiar features found in the kinematical maps, blended in the same group for likely similar origin, non-regular rotators are divided in four sub-classes: not-rotating galaxies, galaxies with complex and irregular rotation pattern, galaxies with kinematically decoupled core and galaxies with two counter-rotating components (Krajnović et al. 2011). In principle, each map could be characterised by a combination of a few of the above features. All features could occur both in NRR and in RR galaxies, since, if the feature is small (relative to $1R_e$), it does not perturb the velocity map in a significant way.

The kinematical classification in RR and NRR is presented in Fig. 1.1, while a more detailed summary is shown in Tab. 1.1.

The distinction between regular and non-regular rotators is clearly evident in the $(V/\sigma, \varepsilon)$ diagram, which quantifies the relative importance of ordered rotation (traced by the mean stellar velocity V) to random motions (traced by the velocity dispersion σ) as a function of the observed, i.e. apparent, ellipticity ε of a galaxy (Binney 1978).

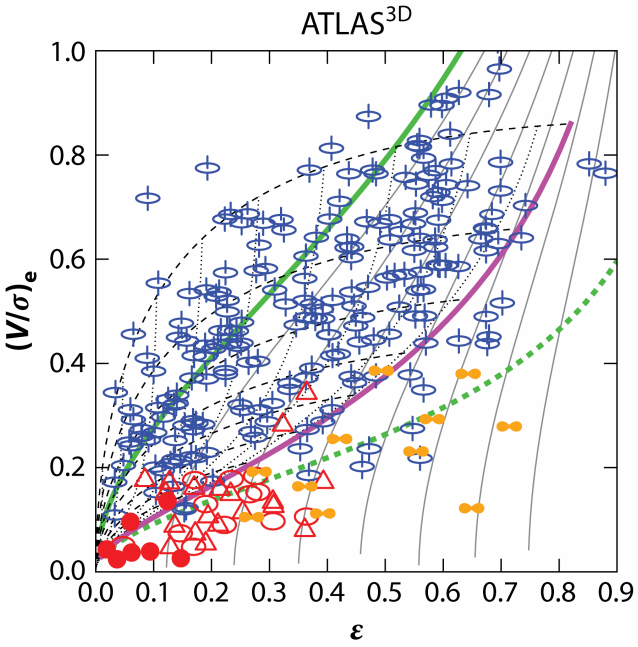

Figure 1.2: The revised $(V/\sigma, \varepsilon)$ diagram. The symbols are the $(V/\sigma, \varepsilon)$ values, where V/σ is the ratio between the ordered stellar rotation V and the random motions σ, and ε is the galaxy observed ellipticity, for 260 ETGs in the ATLAS^{3D} sample, using the symbols introduced in Fig. 1.1. The solid green line is the prediction for an edge-on isotropic rotator, and the thin lines are separated by $\Delta\delta = 0.1$ in anisotropy. The magenta line is the edge-on relation of $\delta \simeq \beta_z = 0.7 \times \varepsilon_{\rm intr}$ (Cappellari et al. 2007), and the dotted lines indicate how this relation transforms at different equally spaced inclinations. Regular rotators (blue symbols) and non-regular rotators (red symbols) can be approximately separated by the line $(V/\sigma)^* = 1/3$ (dashed green line). Taken from Cappellari (2016).

In the diagram, V and σ are luminosity-weighted quantities (within an ellipse that encloses half of the projected total galaxy light) (Binney 2005; Cappellari et al. 2007).

In Fig. 1.2, regular rotators generally show a wide range of observed ellipticity $\varepsilon = 1 - b/a$, where a and b are respectively the major and the minor axis. Non-regular rotators, instead, are distributed only at ellipticity $\varepsilon \lesssim 0.4$ and tend to lie well below the isotropic line in the diagram.

In other terms, regular rotators can be flatter and the flattening is more supported by the rotation, since they often fall close to the edge-on isotropic line; non-regular rotators are rounder and mainly supported by the anisotropy of the velocity dispersion tensor. For a more refined quantitative classification, the explicit inclusion of the roundness criterion allows the identification of ETGs with discs as fast (or regular) rotators, while genuine disc-less slow (or non-regular) rotators are all rounder than $\varepsilon \lesssim 0.4$.

It is worth noting that galaxies with counter-rotating discs are structurally equivalent to regular rotators and should not be classified as slow rotators. They can appear quite flat, as expected because of their disc-like nature. However, unlike regular rotators, the counter-rotating discs in the ATLAS^{3D} sample all lie below the magenta line in the $(V/\sigma, \varepsilon)$ diagram, because they are dominated by tangential anisotropy, as expected given the fact that the two counter-rotating stellar discs strongly increase the random motions in the tangential direction (Cappellari 2016). Moreover, there is no reason to expect a sharp transition between the regular rotators and the counter-rotating discs, because the classification of a galaxy will simply depend on the amount of externally acquired counter-rotating gas (Bois et al. 2011). In this sense, counter-rotating discs are essentially misclassified slow rotators, which instead form a continuous sequence with the rest of the fast rotators (Cappellari 2016).

1.2 Counter-rotating galaxies

Counter-rotation is a kinematical phenomenon that refers to the presence, within a single galaxy, of two distinct components that rotate in opposite directions around the same rotation axis. As a consequence, counter-rotating galaxies belong to the class of multi-spin galaxies, i.e. systems with more than one axis of rotation (Rubin 1994). Compared to other multi-spin galaxies, such as KDC galaxies, 2σ systems are dynamically simpler and generally less massive, typically $M_\star < 5 \times 10^{10}\, M_\odot$ (Krajnović et al. 2015; Cappellari et al. 2013).

The counter-rotating components may coexist on different spatial scales or within the same disc and they can be either gaseous or stellar. Consequently, the phenomenon of counter rotation can be detected in (Corsini 2014):

the inner regions of the galaxy as in the case of the Sa NGC 3593 (Bertola et al. 1996), which is composed by a small bulge, a main stellar disc which contains ≈

80% of the stars and a secondary counter-rotating stellar disc, that dominates the kinematics in the inner kpc and corotates with the disc of ionised and molecular gas;

the outer regions of the galaxy as for the Sab NGC 4826 (M64), that contains two counter-rotating nested discs of ionised, molecular and neutral gas extending out to 1 and 11 kpc, respectively (Brown et al. 1992);

overall the galaxy as in the case of the Sa NGC 3626, where the gaseous component was observed to counter-rotate at all radii with respect to the stars (Ciri et al. 1995).

It is also possible to distinguish different forms of counter rotation depending on the involved components (Corsini 2014):

gas-versus-stars counter rotation occurs when the gaseous disc counter-rotates with respect to the stellar body of the galaxy, as in the case of the SB0 galaxy NGC 4546 (Galletta 1987);

stars-versus-stars counter rotation is observed when two stellar components counter-rotate and, in particular, it can involve bulge (e.g. SA0 NGC 524, Katkov et al. (2011)), bars (e.g. SB0 NGC 2950, Corsini et al. (2003)) or discs (e.g. SB0 NGC 4550, Rubin et al. (1992));

gas-versus-gas counter rotation represents the case where two gaseous discs counter-rotate, as in the S0 galaxy NGC 7332 (Fisher 1994).

The stars-versus-stars counter-rotating systems, named double-sigma (2σ) galaxies in the ATLAS^{3D} project (see Subsec. 1.1.2), exhibit a distinctive double-peaked structure in the line-of-sight velocity distribution (LOSVD) (Krajnović et al. 2011).

Dynamical models based on orbit superposition confirm that these galaxies consist of two counter-rotating stellar discs, each characterised by high specific angular momentum (Cappellari et al. 2007). Given their pronounced flattening and the high angular momentum of both stellar components, in many cases 2σ galaxies are consistent with being composed of two counter-rotating stellar discs of comparable mass. The observed kinematic signatures, such as the degree of rotation in the velocity maps and the shape and separation of the two velocity dispersion peaks, depend on the relative mass and scale length of each disc.

1.2.1 Detection of counter rotation

The detection of a counter-rotating gaseous component is usually straightforward, e.g. it may be addressed by looking at the opposite orientation of the ionised-gas emission lines and stellar absorption lines in 2-dimensional optical spectra (Galletta 1987). On the contrary, unveiling a counter-rotating stellar component requires a detailed

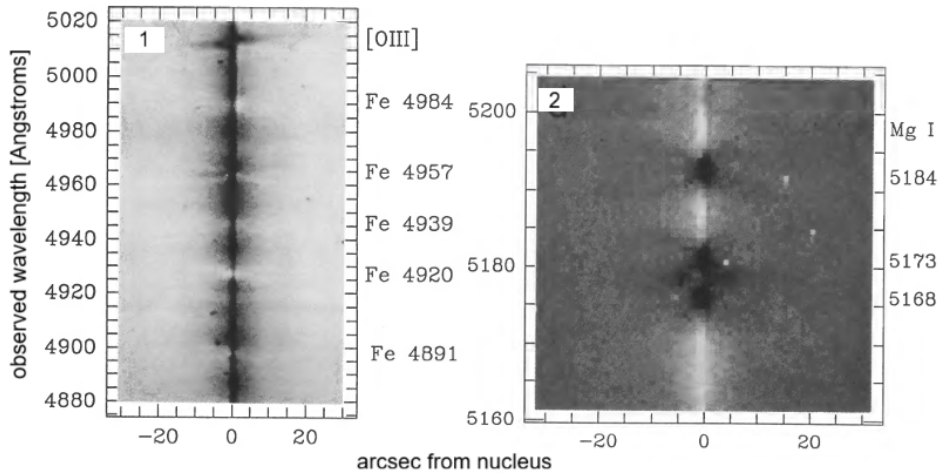

Figure 1.3: Detection of counter-rotating stellar components through the presence of X-shaped absorption lines in NGC 4550 major axis spectrum. *Panel on the left:* for [OIII] emission and several blueward absorption lines, note the X-shaped appearance of the absorption approaching the nucleus, arising from the prograde and retrograde stellar discs. *Panel on the right:* for the MgI triplet, note the two clear absorption rotation components at 5184Å and the complex blending of the 5168 + 5173Å doublet. Adapted from Rubin et al. (1992).

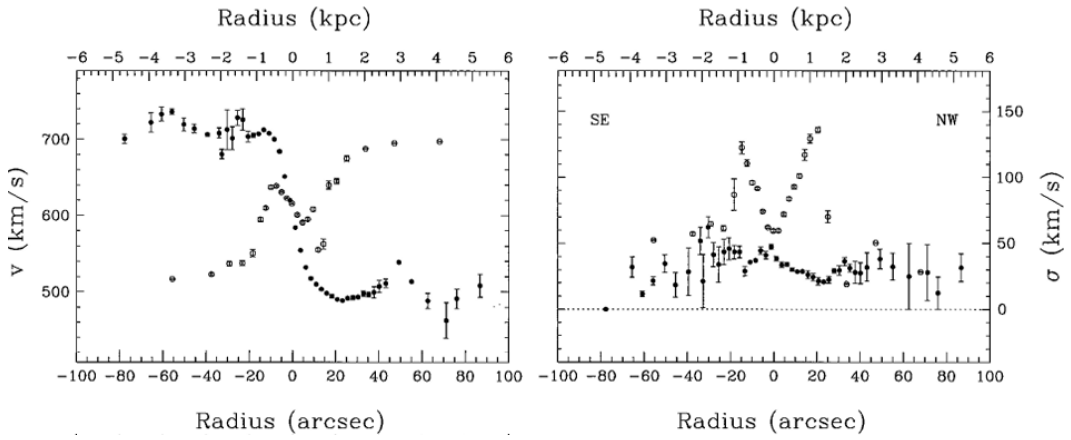

Figure 1.4: Detection of counter-rotating stellar components through kinematical signatures in NGC 3593 major-axis kinematics: open circles denote measurements of the observed velocity and velocity dispersion radial profiles of the stellar component; filled circles denote measurements of the velocity and velocity dispersion of the ionised gas. Adapted from Bertola et al. (1996).

data analysis because the kinematics of two counter-rotating stellar populations are measured from the same absorption lines.

When the two components are photometrically similar, as in the case study of NGC 4550 (Rubin et al. 1992), in the 2-dimensional spectrum X-shaped absorption lines are observed (see Fig. 1.3).

Moreover, for different galaxy properties (i.e. the fraction, dynamical status, and velocity of the retrograde stars with respect to the prograde ones), the superposition of the two components along the line of sight produces a characteristic double-peaked (bimodal) line-of-sight velocity distribution (LOSVD).

More specifically, the presence of two off-centre and symmetric peaks in the stellar velocity dispersion in combination with zero velocity rotation measured along the galaxy major axis is indicative of two counter-rotating discs (Corsini 2014): this particular signature arises because, along the major axis, the mean velocity tends to cancel out where the two counter-rotating components overlap, while the velocity dispersion increases due to the superposition of stars moving in opposite directions. These kinematic features are observed in the radial range where the two counter-rotating components have roughly the same luminosity and their LOSVDs are unresolved (see Fig. 1.4).

1.2.2 Statistical properties of counter-rotating galaxies

Counter rotation is more frequently detected in the gaseous component than in the stars. In the ATLAS^{3D} survey, $(36 \pm 5)\%$ (corresponding to 40/111 objects) of fast-rotating ETGs (ETGs with discs, as defined in Subsec. 1.1.2) present a ionised gas component kinematically misaligned with respect to the stars. This fraction is defined within the population of fast-rotating ETGs and restricted to those objects in this class that have been mapped in molecular gas. The molecular, ionised and atomic gas in all the detected galaxies are always kinematically aligned, even when they are misaligned from the stars, suggesting that all these three phases of the ISM share a common origin (Davis et al. 2011). The occurrence of counter-rotation in the ATLAS^{3D} catalogue is consistent with statistics in previous works, such as $(32^{+19}_{-11})\%$ (at 95% confidence level), corresponding to 17/53 in a sample of S0 galaxies, in Pizzella et al. (2004).

In contrast, stellar counter-rotation is a less frequent phenomenon with respect to gaseous counter-rotation. In ETGs, the occurrence is relatively uncommon, but not negligible.

From Fig. 1.5 is clear that, within the ATLAS^{3D} sample of 260 ETGs, the majority of galaxies have velocity maps dominated by ordered rotation. Only 11 systems ($\approx 4\%$) have been identified as 2σ galaxies (Krajnović et al. 2011), as detailed in Tab. 1.1.

A preliminary estimate of the incidence of stellar counter-rotating galaxies was provided by Kuijken (1996), who found that less than 10% (at 95% confidence level) of S0 galaxies host a significant fraction of counter-rotating stars. This result has

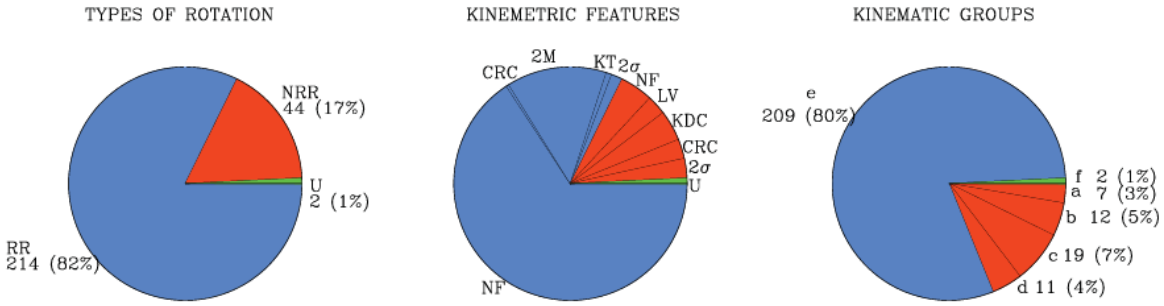

Figure 1.5: Diagrams presenting the kinematic analysis of ATLAS^{3D} galaxies. *On the left:* the frequency of two types of rotators, RRs and NRRs. *At the centre:* the frequency of the kinemetric features. *On the right:* the frequency of the five kinematic groups comprising significant kinemetric features. Letters a–f are explained in Tab. 1.1. Objects which were not classified are represented by the green slice and marked with 'U'. Taken from Krajnović et al. (2011).

been confirmed by more recent work by Gasymov et al. (2025), who analysed a sample of 3576 early-type galaxies from the SDSS-IV MaNGA survey (Bundy et al. 2015) and found that, within the sub-class of S0/S0a galaxies, approximately 3.1% exhibit counter-rotating stellar components.

Importantly, not all 2σ galaxies are classified as non-regular rotators in the ATLAS^{3D} scheme. Four out of eleven exhibit remarkably regular velocity maps, with well-aligned isovelocity contours, and are thus included among regular rotators, despite their distinctive 2σ feature. This highlights that the 2σ phenomenon is not directly tied to the level of ordered rotation but rather to the superposition of two kinematically distinct, dynamically cold components.

1.2.3 Formation scenarios of counter-rotating galaxies

The majority of galaxies hosting counter-rotating components exhibit undisturbed morphologies, showing no clear signs of recent interactions with small satellites or companions of comparable mass. Consequently, if they occur, major mergers take place predominantly in the early stages of a galaxy's evolution, whereas minor mergers may be more recent.

Moreover, the 2σ galaxies environments do not differ significantly from those of normal galaxies, as shown by the statistical analysis of Bettoni et al. (2001). In that study, the authors examined the number, size, and spatial distribution of faint satellites and bright companions, comparing the large-scale surroundings of 49 counter-rotating galaxies with a control sample of 43 non-counter-rotating systems. These results suggest that the mechanisms responsible for counter-rotation must preserve also the density of galaxies in its local environment (Corsini 2014).

The application of spectral decomposition techniques (Coccato et al. 2011; Katkov

et al. 2013) has enabled the detailed investigation of stellar population properties in many 2σ galaxies. These analyses reveal that the counter-rotating disc generally hosts a younger stellar population that co-rotates with the ionised gas, while the main stellar disc is typically older. This indicates that counter-rotating stellar discs likely form in situ from externally accreted gas rather than through the accretion of stars during mergers.

Accordingly, considering the environmental constraints and the stellar population studies, the most widely supported formation scenario for 2σ galaxies involves external gas accretion as a smooth, non-disruptive process in which infalling material settles onto the galactic disc with angular momentum opposite to that of the pre-existing stellar component.

Numerical simulations show that such gas can be acquired from a gas-rich nearby companion, through wet mergers with dwarf galaxies (Thakar et al. 1997), via tidal gas exchange between neighbouring galaxies (Khim et al. 2021; Silćhenko et al. 2023), or from the intergalactic medium via cold accretion, either episodic or prolonged, along cosmic filaments (Thakar et al. 1996; Algorry et al. 2014).

The newly accreted gas settles into the same disc plane but rotates in the opposite direction; subsequent star formation then builds a secondary stellar disc rotating counter to the main one (Thakar et al. 1996). This process naturally explains the observed differences in stellar populations between the two components.

Counter-rotating gaseous discs are found predominantly in S0 galaxies, which are relatively gas-poor systems (Bettoni et al. 2003), while in LTGs the acquired gas is usually swept away by the pre-existing co-rotating gas component. When gas-rich systems, as spiral galaxies, acquire external gas on retrograde orbits, collisions between the new retrograde and pre-existing prograde gas components lead to loss of angular momentum and subsequent infall towards the galaxy centre. A stable counter-rotating gaseous disc can form only if the mass of the accreted retrograde gas exceeds that of the original component (Lovelace et al. 1996). Star formation within this counter-rotating gas subsequently produces a secondary stellar disc. Consequently, a higher fraction of counter-rotating gaseous discs is observed in S0 galaxies than in spirals (Pizzella et al. 2004). The few spirals known to host counter-rotating gaseous and/or stellar discs are all very early-type systems (S0/a–Sa) (Corsini 2014; Sandage et al. 1994).

Although external gas accretion appears to be the dominant mechanism, other, but less common, processes may also produce counter-rotating structures.

Usually, major mergers between disc galaxies with comparable masses are ruled out because they tend to produce ellipticals. Anyway, for a narrow range of initial conditions (finely tuned orbits that preserve the disc structure), major mergers are successful in building a remarkably axisymmetric disc which hosts two counter-rotating stellar components of similar mass and size (Puerari et al. 2001; Crocker et al. 2009).

Internal dynamical phenomena such as bar dissolution, resonant orbit families, or disc instabilities can generate localised counter-rotation without the need for external accretion (Evans et al. 1994). However, these internal processes generally give rise to counter-rotating cores rather than large-scale discs, and therefore cannot account for extended 2σ systems. Moreover, they cannot explain the observed differences in stellar populations, particularly the significant age differences between stellar components.

Chapter 2

Properties and observational data of NGC 1366

In this chapter we focus on the lenticular galaxy NGC 1366, providing a detailed overview of its general properties and summarising previous analyses from Morelli et al. (M08), Morelli et al. (M15), and Morelli et al. (M17). The chapter is organised as follows: Sec. 2.1 summarises the main characteristics of the galaxy, Sec. 2.2 describes the photometric properties, Sec. 2.3 presents the kinematic analysis, and Sec. 2.4 discusses the stellar population properties.

2.1 General properties

NGC 1366 (`RA 03:33:53.69, Dec -31:11:38.87`, $z = 0.004$, from the NASA/IPAC Extragalactic Database (2025)) is a bright spindle-shaped S0 galaxy (Fig. 2.1) in the Fornax cluster. Due to its high inclination, the disc of NGC 1366 is observed nearly edge-on. Photometric observations reveal that the galaxy exhibits a regular and undisturbed morphology. Although it is classified as a member of the LGG 96 group, the absence of nearby bright companions suggests that it has not undergone any recent significant interaction.

It is classified as $S0^0$ according to the classification of Vaucouleurs et al. (1991) and as $S0_1$/E7 by Sandage et al. (1994), due to its highly inclined thin disc.

For consistency with the analyses by M08, M15 and M17, it is adopted $D = 17\,\mathrm{Mpc}$ (Ferguson 1989). Consequently, the scale conversion $1\,\mathrm{arcsec} = 0.0824\,\mathrm{kpc}$ is used throughout this work.

The apparent total R-band magnitude of NGC 1366 is $m_R = 11.49\,\mathrm{mag}$ (Lauberts et al. 1989), which at a distance of 17 Mpc corresponds to an absolute total R-band magnitude $M_R^0 = -19.66\,\mathrm{mag}$.

The main structural and photometric parameters of NGC 1366 are summarised in Tab. 2.1.

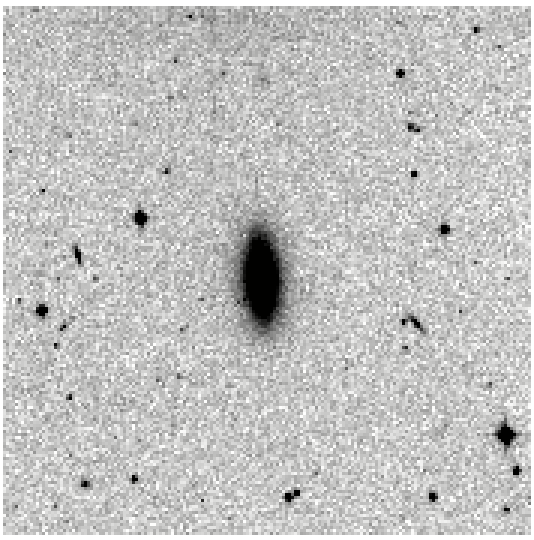

Figure 2.1: Optical R-band image of NGC 1366, acquired with the ESO 1.0 m telescope. The field of view (FOV) is $7.94 \times 7.94\,\mathrm{arcmin}^2$ and the image resolution is 2 arcsec. Taken from NASA/IPAC Extragalactic Database (2025).

Galaxy	Type (RC3)	T (RC3)	$D_{25} \times d_{25}$ [arcmin]	m_R [mag]	D [Mpc]	M_R^0 [mag]
(1)	(2)	(3)	(4)	(5)	(6)	(7)
NGC 1366	$S0^0$	-2.0	2.1×0.9	11.49	17.0	-19.66

Table 2.1: Main properties of NGC 1366, adapted from Table 1 of M08. Columns description: (2) morphological classification from RC3; (3) numerical morphological type from RC3; (4) apparent isophotal diameters measured at a surface brightness level of $\mu_B = 25\,\mathrm{mag\,arcsec}^{-2}$ from RC3; (5) total observed R-band magnitude from RC3; (6) distance obtained as luminosity-weighted mean radial velocity (Garcia 1993) divided by $H_0 = 75\,\mathrm{km\,s}^{-1}\,\mathrm{Mpc}^{-1}$; (7) absolute total R-band magnitude, adopting D.

2.2 Photometry

The photometric properties of NGC 1366 were analysed in detail by M08. The analysis was performed on R-band (Bessel R-band centred at 6431 Å) photometric images. The observations were carried out in two runs at the European Southern Observatory (ESO) in La Silla (Chile), with the ESO 3.6-m Telescope using the ESO Faint Object Spectrograph and Camera 2 (EFOSC2).

The galaxy surface brightness distribution is well reproduced by the sum of the contributions of a bulge and a disc component: it was fitted by means of a two-component model consisting of a Sérsic bulge and an exponential disc. The adopted decomposition yielded a good representation of the light distribution across the whole image.

Let the (x, y) plane be the plane of the sky, with the x-axis parallel to direction of right ascension (pointing westward), the y-axis parallel to direction of declination (pointing northward) and the z-axis along the line-of-sight (pointing toward the observer). Bulge and disc isophotes are ellipses centred on (x_0, y_0), with constant axial ratio q_i and constant position angle $\mathrm{PA_i}$. The galaxy inclination is derived as

$$i = \arccos q_d = 65.80^\circ. \tag{2.1}$$

The surface brightness distribution of the bulge is described by a Sérsic law (Sérsic 1968), given by

$$I_b(x, y) = I_e \exp\left\{-b_n\left[\left(\frac{r_b}{R_e}\right)^{1/n} - 1\right]\right\}, \tag{2.2}$$

where R_e, I_e, n, and b_n are respectively the effective radius, the surface brightness at R_e, the Sérsic index and the Sérsic constant (see Subsec. 1.1.1). The radius r_b is given by

$$\begin{aligned} r_b = &[(-(x - x_0)\sin \mathrm{PA_b} + (y - y_0)\cos \mathrm{PA_b})^2 + \\ &(-(x - x_0)\cos \mathrm{PA_b} - (y - y_0)\sin \mathrm{PA_b})^2/q_b^2]^{1/2}. \end{aligned} \tag{2.3}$$

The surface brightness distribution of the disc follows a standard exponential decline (Freeman 1970), with a relatively large scale length, typical of lenticular galaxies:

$$I_d(x, y) = I_0 e^{-r_d/h}, \tag{2.4}$$

where I_0 is the central surface brightness and h is the disc scale length. The radius r_d is given by:

$$\begin{aligned} r_d = &[(-(x - x_0)\sin \mathrm{PA_d} + (y - y_0)\cos \mathrm{PA_d})^2 + \\ &(-(x - x_0)\cos \mathrm{PA_d} - (y - y_0)\sin \mathrm{PA_d})^2/q_d^2]^{1/2}. \end{aligned} \tag{2.5}$$

Component	R_e or h [arcsec]	R_e or h [kpc]	n	q	PA [deg]
(1)	(2)	(3)	(4)	(5)	(6)
Bulge	2.59 ± 0.07	0.213 ± 0.006	1.5	0.80 ± 0.01	5.38 ± 2.40
Disc	12.81 ± 0.32	1.055 ± 0.026	1.0	0.41 ± 0.01	2.08 ± 2.32

Table 2.2: Structural parameters for bulge and disc of NGC 1366, adapted from Table 2 of M08. Columns description: (2) effective radius R_e of the bulge and scale length h of the disc in arcsec; (3) effective radius R_e of the bulge and scale length h of the disc in kpc; (4) shape parameter n; (5) axial ratio of the isophotes q; (6) position angle of the major axis PA.

The photometric parameters in M08 were derived fitting iteratively a model of the surface brightness $I_m(x, y) = I_b(x, y) + I_d(x, y)$ to the pixels of the galaxy image and the results are reported in Tab. 2.2.

The result of the photometric decomposition of the surface brightness distribution is shown in Fig. 2.2.

Derivation of the luminosities for the two-component model

This study reproduce in Fig. 2.3 the model for the observed surface brightness distribution (left panel in Fig. 2.2), using the parameters in Tab. 2.2, with a Sérsic profile ($n = 1.5$) for the bulge and an exponential disc:

$$\mu_b(R) = \mu_{e,b} + 2.5 b_n \log(e) \left[\left(\frac{R}{R_e} \right)^{1/n} - 1 \right] \tag{2.6}$$

$$\mu_d(R) = \mu_{0,d} + 2.5 \log(e) \left(\frac{R}{h} \right) \tag{2.7}$$

The values of effective surface brightness of the bulge $\mu_{e,b}$ and central surface brightness of the disc $\mu_{0,d}$ have been measured from the modelled radial profile and they are reported in Tab. 2.3.

Let us consider a system described by a Sérsic profile with index n_i and apparent axis ratio q_i. The total luminosity of the system is derived as a generalisation of the classical Sérsic profile integration (Ciotti 1991), where the projected light of an axisymmetric ellipsoid is recovered as

$$L_i = 2\pi q_i R_{e,i}^2 I_{0,i} n_i \frac{\Gamma(2n_i)}{b_{n_i}^{2n_i}}, \tag{2.8}$$

where $R_{e,i}$ is the effective radius of the system, $I_{0,i}$ its central surface brightness and $\Gamma(2n_i)$ is the complete gamma function. In the limit $q_i = 1$, the expression reduces

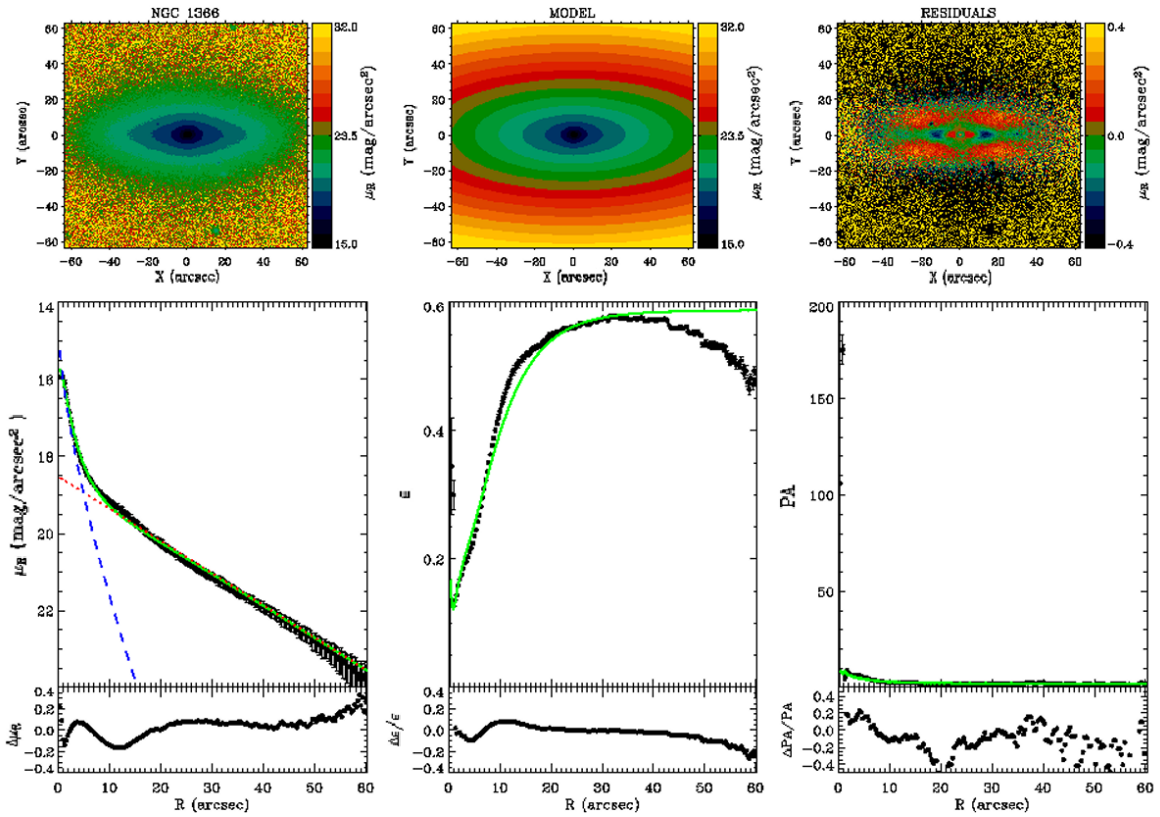

Figure 2.2: Two-dimensional photometric decomposition of the galaxy in R-band. *Upper panels (from left to right)*: map of the observed, modelled and residual (observed-modelled) surface brightness distribution, rotated to have the galaxy major axis parallel to rows. *Lower panels (from left to right)*: ellipse-averaged radial profile of surface brightness, ellipticity and position angle measured in the observed (dots with error bars) and modelled image (solid line). The dashed and dotted lines represent the surface brightness contribution of the bulge and disc, respectively. The difference between the ellipse-averaged radial profiles extracted from the observed and modelled images is also shown. Taken from M08.

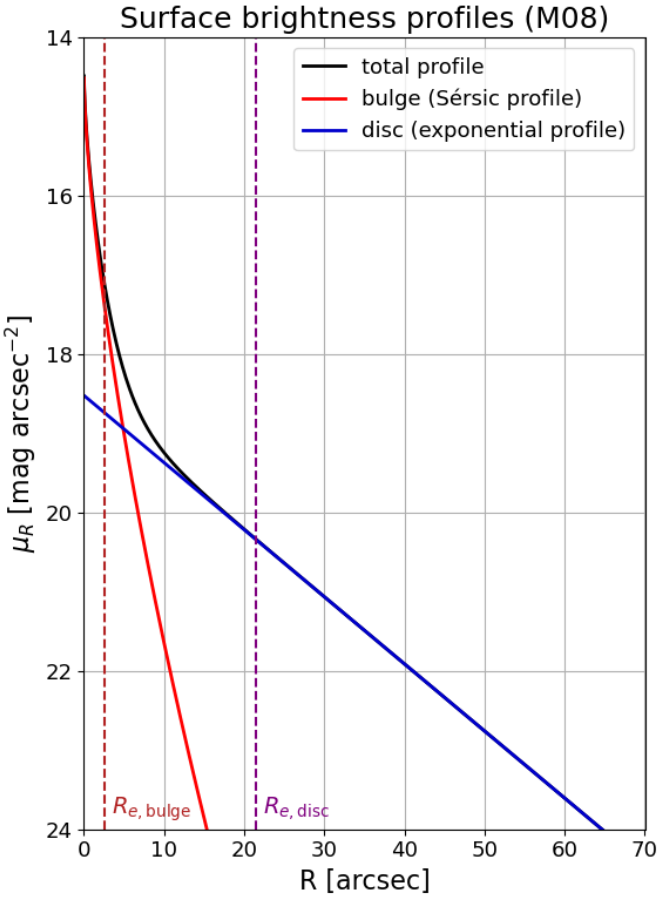

Figure 2.3: Two-component model for the radial profile of the surface brightness $\mu_R(R)$ of NGC 1366, constructed from the surface brightness distribution observed in R-band and reproduced in Fig. 2.2 from M08.

to the standard circular case.

A fundamental relation arises considering that for flattened systems it is convenient to define the elliptical radius as

$$\eta = \sqrt{\frac{R^2}{R_e^2} + \frac{z^2}{q^2 R_e^2}}, \tag{2.9}$$

where R and z are the cylindrical coordinates and q is the flattening of the system. Then, the Sérsic law is written as

$$I(\eta) = I_e \mathrm{e}^{-b_n(\eta^{1/n}-1)}. \tag{2.10}$$

By evaluating the profile at $\eta = 0$, one finds the relation between I_0 and I_e as

$$I_0 = I_e \mathrm{e}^{b_n}. \tag{2.11}$$

The luminosity of the bulge is derived from the effective surface brightness of the bulge $\mu_{e,b}$ (in Tab. 2.3), starting from the surface brightness (in luminosity per unit area):

$$I_{e,b} = 10^{-0.4(\mu_{e,b}-\mu_{R,\odot})} = 2.81 \times 10^9 \ L_{R,\odot}\mathrm{kpc}^{-2}, \tag{2.12}$$

where the photometric zero point $\mu_{R,\odot}$ is the solar surface brightness in the R-band, obtained from $\mu_{R,\odot} = M_{R,\odot} + 2.5\log(206265^2) \approx 26.03$ mag/arcsec^2, where $M_{R,\odot} = 4.458$ mag is the absolute magnitude of the Sun in the R-band (Binney et al. 1998), and the factor $2.5\log(206265^2)$ converts the flux from units of $L_\odot/\mathrm{pc}^2$ to magnitudes per arcsec^2. Then, using using Eq. 2.11,

$$I_{0,b} = I_{e,b}\mathrm{e}^{b_n} = 4.06 \times 10^{10} \ L_{R,\odot}\mathrm{kpc}^{-2}, \tag{2.13}$$

and finally, known the flattening q_b and the effective radius $R_{e,b}$ (in Tab. 2.2),

$$L_b = 2\pi q_b R_{e,b}^2 I_{0,b} n_b \frac{\Gamma(2n_b)}{b_{n_b}^{2n_b}} = 1.46 \times 10^9 \ L_{R,\odot} \tag{2.14}$$

The luminosity of the disc is derived from the central surface brightness of the disc $\mu_{0,d}$ (in Tab. 2.3), starting from the surface brightness:

$$I_{0,d} = 10^{-0.4(\mu_{0,d}-\mu_{R,\odot})} = 1.01 \times 10^9 \ L_{R,\odot}\mathrm{kpc}^{-2} \tag{2.15}$$

and then, known the flattening q_d and the disc scale length h (in Tab. 2.2), using $R_e \approx 1.678h$ (for the case $n = 1$) (Graham et al. 2005),

$$L_d = 2\pi q_d R_{e,d}^2 I_{0,d} n_d \frac{\Gamma(2n_d)}{b_{n_d}^{2n_d}} = 2.90 \times 10^9 \ L_{R,\odot} \tag{2.16}$$

The parameters and derived luminosities of the modelled surface brightness profile are collected in Tab. 2.3.

Component	μ_e or μ_0 [mag/arcsec^2]	L_R [$10^9 L_{\odot,R}$]	$L/L_{\rm tot}$
Bulge	17.41	1.46	0.33
Disc	18.52	2.90	0.67

Table 2.3: Effective surface brightness of the bulge and central surface brightness of the disc, luminosities and fraction of total luminosity for bulge and disc of NGC 1366, derived from the photometric modelling of M08.

2.3 Kinematic analysis

The analysis in M08 was performed on spectra acquired along the galaxy major axis. The spectroscopic observations were carried out in three runs at ESO in La Silla (Chile), where the ESO 3.6-m Telescope mounted the EFOSC2 spectrograph and the New Technology Telescope (NTT) mounted the ESO Multi-Mode Instrument (EMMI) (see M08). From the spectrum, the line-of-sight velocity distribution (LOSVD) along the slit was derived, then the radial velocity v and the velocity dispersion σ were measured. At each radius, they have been derived by fitting the LOSVD with a Gaussian. The errors on the radial velocity v and the velocity dispersion σ were derived from photon statistics and CCD read-out noise, calibrating them by Monte Carlo simulations.

The measured stellar kinematics (in Tab. 2.4) highlights the presence of a peculiar behaviour, with an inversion of the sign of the rotational velocity in the inner region. Thus M08 suggests the presence of two counter-rotating components: the bulge and the disc of the galaxy.

2.3.1 Spectral decomposition of counter-rotating discs

M17 carried out a long-slit spectroscopic study of NGC 1366, extending the analysis previously conducted by M08. Their spectroscopic observations were carried out at ESO in La Silla (Chile), with the New Technology Telescope (NTT).

The analysis was performed on spectra acquired along the galaxy major and minor axis and along both of them the stellar kinematics were derived with a single-component and with a two-components analysis.

The single-component analysis confirms the results in M08, since the rotation curve is consistent with the one in the previous work (Fig. 2.4).

No kinematic signature of stellar decoupling was found along the minor axis of NGC 1366, while a peculiar stellar kinematics is observed along the major axis: the combination of zero velocity with two off-centred and symmetric peaks in the stellar velocity dispersion is indicative, as discussed in Subsec. 1.2.1, of the presence of two counter-rotating components in the outer disc. In this thesis, discussing the disc decomposition, the component rotating in the same direction as the bulge is defined as

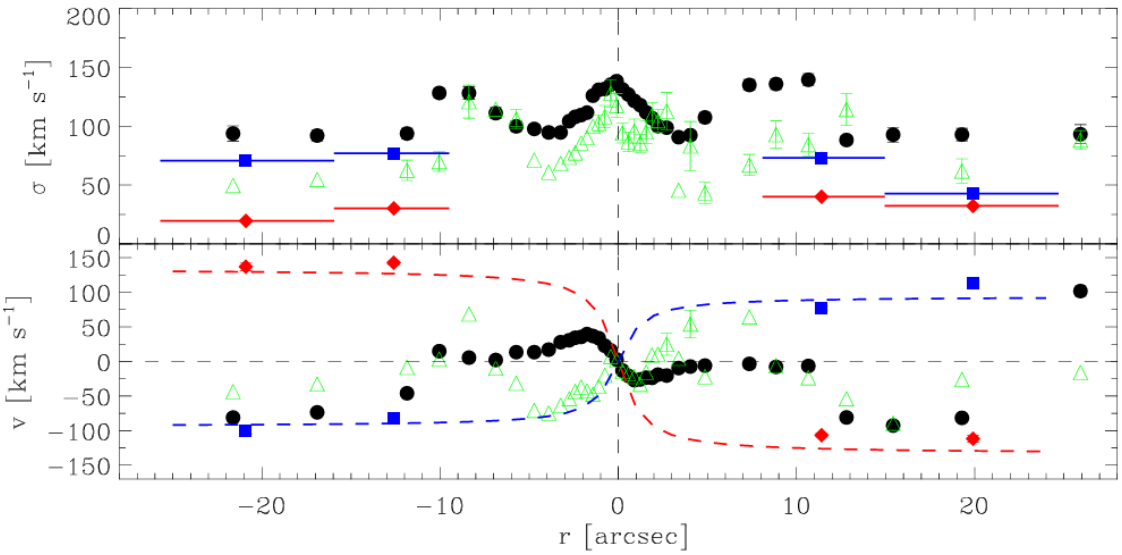

Figure 2.4: Line-of-sight velocity dispersion *(top panel)* and velocity *(bottom panel)* radial profiles measured along the major axis of NGC 1366 for the total (black filled circles), counter-rotating (blue filled square), and co-rotating (red filled diamonds) stellar components and for the ionised gas component (green open triangles). Error bars smaller than symbols are not shown. The blue and red horizontal lines in the top panel mark the radial bins adopted for measuring the counter-rotating and corotating components, respectively. The blue and red dashed lines in the bottom panel are a tentative indication of the velocity rotation curves for the counter-rotating and corotating component, respectively. Taken from M17.

R [arcsec]	V [km/s]	σ [km/s]
-27.6	50.1 ± 41.3	141.6 ± 29.4
-16.5	6.4 ± 17.6	198.4 ± 22.2
-9.5	-7.0 ± 10.0	186.9 ± 15.0
-5.3	-10.4 ± 7.7	170.8 ± 11.4
-3.0	-18.1 ± 10.5	168.2 ± 9.2
-1.8	-20.7 ± 7.4	167.6 ± 9.1
-1.0	-17.7 ± 5.8	167.0 ± 8.1
-0.6	-7.5 ± 9.0	188.3 ± 12.5
-0.3	-6.1 ± 7.7	186.6 ± 11.1
0.0	4.5 ± 8.0	195.7 ± 11.3
0.3	9.4 ± 9.0	202.7 ± 11.9
0.6	14.3 ± 4.2	156.6 ± 6.6
0.9	22.3 ± 8.3	195.9 ± 11.9
1.3	24.3 ± 6.7	179.7 ± 10.8
2.1	15.6 ± 9.3	171.1 ± 11.7
3.3	13.3 ± 12.4	170.7 ± 14.0
5.6	-5.4 ± 8.3	164.9 ± 10.5
9.8	-2.4 ± 11.6	181.6 ± 22.1
16.8	-3.9 ± 7.9	177.2 ± 13.2
27.9	-60.8 ± 48.5	173.8 ± 35.8

Table 2.4: Stellar kinematic of NGC 1366 in M08. The columns show the radius along the major axis, the rotation velocity along the major axis, and the velocity dispersion. Taken from M08.

the co-rotating disc component, while the other, rotating in the opposite direction, is defined as the counter-rotating disc component. In M17, to investigate the presence of counter rotation, the spectrum is analysed only in two radial bins centred at $R \approx 1$ kpc

Component	Age [Gyr]	$[Z/H]$ [dex]
Bulge	5.1 ± 1.7	0.39 ± 0.08

Table 2.5: The central values of age and metallicity derived in M08. Adapted from M08.

and $R \approx 2$ kpc. The spectroscopic decomposition returns the line-of-sight velocity v and velocity dispersion σ of the two stellar components only in these selected positions, as shown in Fig. 2.4 (blue and red points): the two counter-rotating stellar components have high rotation velocity and low velocity dispersion ($V/\sigma \simeq 2$) and give almost the same contribution to the galaxy luminosity. It is important to stress that no actual rotation curve is derived here; the lines shown merely provide a tentative indication based on the four available datapoints. As discussed in M17, the limited spatial sampling prevents a robust reconstruction of the rotational behaviour of the stellar components, and therefore the plotted trend should be interpreted only as a qualitative guide rather than a physically constrained rotation curve.

Moreover, the constant slope of the exponential surface brightness radial profile outside the bulge-dominated region suggests that the two counter-rotating components in the disc have a similar scale length.

Therefore, kinematic and photometric properties support the disc nature of the two counter-rotating components in the outskirts (M17).

2.4 Stellar population studies

2.4.1 Bulge and disc stellar populations

In M08, central values of line-strength indices were derived from the major-axis spectrum. From these, age and metallicity of the stellar population of the bulge were obtained, using the stellar population models by Thomas et al. (2003), that predict the values of the line-strength indices for a single stellar population as function of the age, metallicity and $[\alpha/Fe]$ ratios. The values are listed in Tab. 2.5.

Moreover, M08 observes that NGC 1366 shows a steep positive age gradient (from about 5 to 11 Gyr) and a strong negative metallicity gradient (from about 0.5 to 0 dex) within 5 arcsec from the centre (corresponding to $R \lesssim 0.41$ kpc). The peculiar radial gradients observed for the stellar population of the inner region provided a first hint of the presence of a sub-structure (M08).

M15 investigates the properties of the stellar population in the disc of NGC 1366 using long-slit spectroscopy along the major axis, with the technical specifics already mentioned in M08.

Measuring the stellar populations of different galaxy components from integrated spectra is affected by contamination: the properties inferred for one component can be

Component	Age [Gyr]	[Z/H] [dex]
Disc	7.6 ± 0.8	-0.26 ± 0.03

Table 2.6: Values of age and metallicity in the disc-dominated region (at the radius where the disc contributes more than 95% of the galaxy surface brightness) derived in M15. Adapted from M15.

biased by the others, depending on their relative contribution to the galaxy's surface brightness. This is particularly critical for bulges and bars, which are always embedded in discs and overlap at small radii. Discs, however, can be reliably studied at larger radii where they dominate the surface brightness. M15 then studies the disc-dominated region between r_{d95}, the radius where the disc contributes more than 95% of the galaxy's surface brightness, and $r_{\rm last}$, the outermost radius with sufficient signal-to-noise ratio to measure stellar population properties. The corresponding spectrum was fitted using MILES stellar population models (Sánchez-Blázquez et al. 2006), to derive luminosity-weighted ages and metallicities for the stellar component of the disc. The values are listed in Tab. 2.6.

Moreover, M15 found in the disc the presence of two stellar populations with distinct ages. The stellar population of the disc is dominated by an old component (12.5 ± 1.1 Gyr), but in addition a younger sub-population (1.1 ± 0.3 Gyr) was detected, especially toward the outer regions, suggesting that the disc has experienced a recent episode of star formation, possibly due to external gas accretion. The metallicity gradient of the disc is slightly negative, in line with an inside-out growth scenario (M15).

2.4.2 Disc counter-rotating components stellar populations

In order to better investigate the different stellar populations in the disc, M17 applied a two-components analysis to the major-axis spectrum of NGC 1366. The measured Lick line-strength indices of the corotating and counter-rotating components on the best-fitting synthetic templates were compared with single stellar population (SSP) models, to infer luminosity-weighted ages, metallicities, and α-element abundance ratios.

A striking difference emerges between the main and secondary discs, indicating distinct formation epochs and chemical enrichment histories and suggesting a general picture consistent with other examples of 2σ galaxies (see Sec. 1.2). The comparison of the age values suggests that the counter-rotating component is significantly younger than the corotating component, which instead is characterised by an age consistent with that of bulge. The subsolar metallicity and almost solar α/Fe enhancement of the corotating component suggests a formation timescale of few Gyr, that occurred at the time of the galaxy assembly. The counter-rotating stellar component, with lower α/Fe enhancement and subsolar metallicity, can be the end result of a slower star formation

process, occurred in a disc of accreted gas.

Formation scenario and ionised gas dynamics

The stellar population associated with the corotating component exhibits an old age, consistent with that of the bulge, together with subsolar metallicity and nearly solar α/Fe enhancement. These properties suggest a formation over a relatively short timescale of a few gigayears, likely coinciding with the main epoch of galaxy assembly.

In contrast, the counter-rotating stellar component is significantly younger and characterised by subsolar metallicity and a lower α/Fe ratio. This component may have formed through a more prolonged star formation episode within a gaseous disc accreted by a pre-existing galaxy and subsequently settled onto retrograde orbits (see Subsec. 1.2.3).

Unlike most previously studied systems, however, studies in M17 show that the ionised gas in NGC 1366 is not dynamically coupled to the counter-rotating stellar component. Its complex kinematics, featuring multiple velocity components along the minor axis and distinct gas clouds along the line of sight, indicate a more intricate evolutionary history. The observed kinematic decoupling between the ionised gas and the counter-rotating stars challenges the simple scenario of gas accretion followed by in-situ star formation.

A plausible scenario involves episodic gas accretion, already analysed in Thakar et al. (1996). In the specific case of NGC 1366, the first event, occurring approximately 3 Gyr ago, likely led to the formation of the counter-rotating stellar component. This was followed by a more recent accretion episode, which appears to be still ongoing.

However, this raises the question of the origin of the newly acquired, kinematically decoupled gas, as there is no obvious donor galaxy in the immediate vicinity of NGC 1366. One possible explanation is that the gas originates from small clouds either within the galaxy itself or from the surrounding environment. When external gas is captured in discrete clouds, it can settle onto the galaxy disc over relatively short timescales. In this context, NGC 1366 may represent a system observed during an intermediate stage of the accretion process, prior to reaching a dynamically stable configuration (M17).

An alternative scenario was explored by Crocker et al. (2009), who used numerical simulations to study the time evolution of gas and stellar kinematics in the formation of the counter-rotating discs of NGC 4550 via a binary merger. About 1 Gyr after the merger, the stars form two settled counter-rotating discs, while the gas remains kinematically disturbed. By 1–2 Gyr, the gas tends to settle into a more regular configuration. The structural and stellar population properties of NGC 1366 differ from those of NGC 4550, so dedicated simulations are required to assess the role of a binary merger in its formation.

M17 conclude that the present-day configuration of NGC 1366 preserves a clear signature of past gas accretion, which built the counter-rotating stellar disc. The differences in age, metallicity, and abundance ratios between the two components retain the imprint of their separate evolutionary histories.

Chapter 3

Numerical implementation of multicomponent modelling

This chapter presents the numerical framework adopted to construct multicomponent dynamical models of axisymmetric galaxies using the code `JASMINE2`, that solves the two Jeans equations in cylindrical coordinates for axisymmetric, stationary, and collisionless multi-component systems.

Sec. 3.1 introduces the general structure of the code, the theoretical foundations of the modelling procedure implemented, and the underlying scaling-based strategy, which separates the modelling procedure into a Potential and Jeans Solver (P&JS) and a Post-Processing (PP) stage.

The construction of the axisymmetric dynamical multicomponent galaxy models used throughout this work is described in Sec. 3.2, while Sec. 3.3 summarises the numerical parameters adopted at different stages of the modelling pipeline. The solution of the Jeans equations for multiple stellar components, implemented within `JASMINE2`, is presented in Sec. 3.4.

The PP stage, detailed in Sec. 3.5, outlines the full procedure applied to the output of a dedicated `JASMINE2` run (i.e. execution). This includes the assignment of mass and luminosity weights, the kinematical decomposition of azimuthal motions, the projection of model quantities along a line of sight, and the final composition of the produced morphological and kinematical fields, with the rescaling to physical units. In the framework of this thesis, the PP workflow makes use of several routines already present, some of which were adapted to the specific requirements of this study. In addition, a dedicated block of code was developed to be executed at the end of the PP pipeline. This new module handles the weighting scheme and produces the final projected photometric and kinematic fields.

In this thesis, the code `JASMINE2` is employed to generate a family of dynamical models that serve as the basis for a dedicated post-processing analysis. The post-processing stage is carried out using routines specifically developed for this work, which

allow the dynamical parameters, mass and luminosity weights, and physical scales to be varied systematically. The objective is to construct a dynamical model tailored to the galaxy NGC 1366.

Although JASMINE2 provides a general modelling framework, capable, for instance, of incorporating additional mass components such as a dark matter (DM) halo or a central black hole (BH), the present study focuses on a two-component stellar configuration consisting of a bulge and a disc. Each stellar component is described implicitly through a two-integral distribution function, consistent with the axisymmetric nature of the system. This restricted but physically motivated setup, described in the following sections, reflects the specific aims of the modelling procedure undertaken in this thesis.

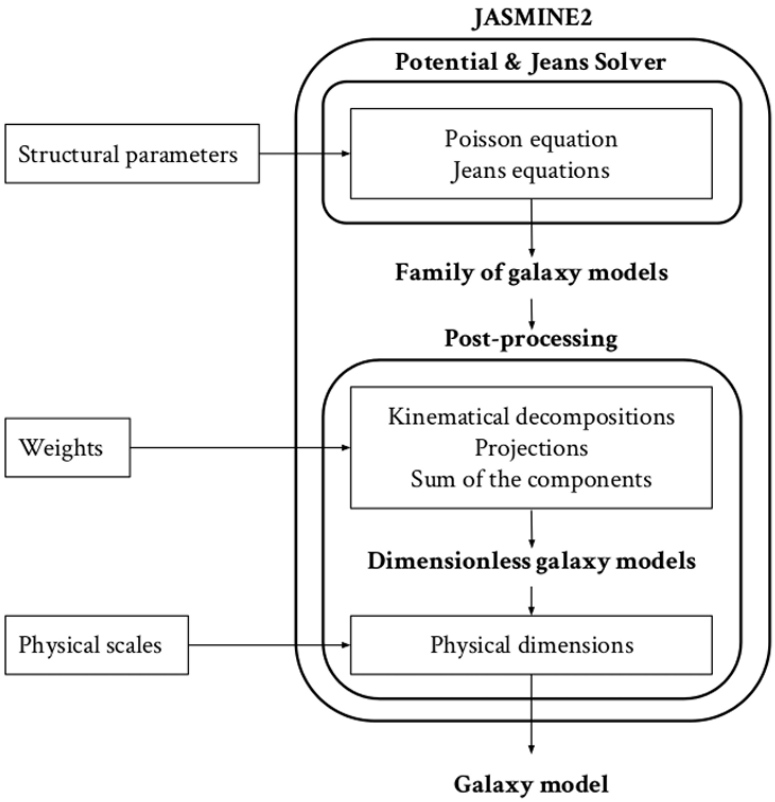

Figure 3.1: Scheme of modelling procedure. The diagram summarises the procedure of construction of multicomponent galaxy models, based on the scaling approach implemented in the code JASMINE2. Taken from Caravita (2022).

3.1 The numerical code JASMINE2

The numerical code JASMINE2 (Caravita 2022; Caravita et al. 2021), an upgraded version of the original code JASMINE (Jeans AxiSymmetric Models of galaxies IN Equi-

librium) (Posacki 2014; Posacki et al. 2013), is designed to construct dynamical models of stationary, axisymmetric galaxies by solving the Jeans equations for multiple stellar components embedded in a composite gravitational potential.

The code is organised into two main modules, as illustrated in Fig. 3.1: the Potential and Jeans Solver (P&JS), written in `Fortran90`, and the Post-Processing (PP), developed in `Python`. In the P&JS module, the gravitational potential associated with each density component is computed and the Jeans equations are solved for every stellar component within each potential contribution. The results are stored in binary HDF5 files and expressed as normalised (i.e. dimensionless) and scaled (i.e. not multiplied by the relative mass fraction) quantities, hereafter referred to as tilde quantities.

The PP module performs the subsequent stages of the modelling pipeline. Once the mass and luminosity weights have been assigned, the kinematical decomposition is applied, followed by the projection of the resulting fields and the combination of the different components. This process produces the dimensionless quantities weighted according to their respective mass ratios. In the final stage, the appropriate physical scales are introduced to recover the physical dimensions and units of the complete galaxy model.

3.2 Structure of the galaxy models

Since the numerical code `JASMINE2` models axisymmetric, stationary stellar systems as multicomponent configurations, in the more general case these models may include N distinct stellar components, together with additional mass contributions such as a dark matter halo (h) and a central supermassive black hole (BH). For the 2-component modelling of the galaxy NGC 1366, only two stellar components are considered.

Adopting cylindrical coordinates (R, ϕ, z), with the symmetry axis aligned along the z-axis, each stellar component is characterised by a set of structural parameters that define its continuous density distribution $\varrho_{*i}(R, z)$. The total stellar density ϱ_* and the total stellar mass M_* of the system can then be expressed as

$$\varrho_*(R, z) = \sum_i \varrho_{*i}, \qquad M_* = \sum_i M_{*i}, \qquad i = 1, ..., N, \tag{3.1}$$

where the index i denotes the sum over the N stellar components.

Under the assumption that each stellar density distribution ϱ_{*i} corresponds to a simple stellar population (Renzini et al. 1996; Maraston 2005), i.e. an idealised assembly of stars all formed at the same time, from gas of uniform chemical composition and evolving passively thereafter, each ϱ_{*i} is associated with stars sharing the same age, initial mass function and mass-to-light ratio Υ_{*i}. The luminosity density and total luminosity of the i-th stellar component are therefore given by

$$\nu_{*i}(R, z) = \frac{\varrho_{*i}}{\Upsilon_{*i}}, \qquad L_{*i} = \frac{M_{*i}}{\Upsilon_{*i}}. \tag{3.2}$$

Potential & Jeans Solver (structural parameters for the scaled stellar densities $\tilde{\varrho}_{*i}$)	Sérsic indices	n_i
	shape parameters	q_i
	scale-length ratios	$x_i = \frac{r_{*i}}{r_*}$
Post-Processing (weights)	stellar luminosities	L_{*i}
	mass-to-light ratios or mass fractions	Υ_{*i} or R_i
	kinematical decompositions	$k_i = \lambda_i \delta_i$
Post-Processing (physical scales)	total stellar mass	M_*
	stellar scale-length	r_*

Table 3.1: Model parameters (for the particular case of this work) entering the three main steps involved in constructing a multicomponent galaxy model, listed from top to bottom in the order in which they are considered in the numerical implementation in the code `JASMINE2`. Adapted from Caravita et al. (2021).

Treating the total stellar distribution ϱ_* as a composite stellar population composed of all ϱ_{*i}, the corresponding total luminosity density and total luminosity are

$$\nu_*(R,z) = \sum_i \nu_{*i}, \qquad L_* = \sum_i L_{*i}. \tag{3.3}$$

The mass density distribution, in turn, defines the gravitational potential that governs the dynamics of the system. Each component of the system is treated as a tracer of the total potential: conceptually, every component contributes independently to the overall dynamics, but all components share the same gravitational potential, thereby ensuring the self-consistency of the model.

Through the Poisson equation, the total stellar density yields the corresponding gravitational potential as

$$\nabla^2 \Phi = 4\pi G \varrho_*, \qquad \Phi(R,z) = \sum_i \phi_{*i}, \tag{3.4}$$

where ϕ_{*i} (R, z) is the potential produced by the stellar density ϱ_{*i}.

3.3 Model parameters

Each section of the code requires a specific set of input parameters, as illustrated in Fig. 3.1. Accordingly, the model parameters are organised into three distinct groups, based on their roles in the construction of a multicomponent galaxy model.

These three groups of parameters are discussed here in the order in which they are implemented in `JASMINE2` and are summarised in Tab. 3.1.

3.3.1 Structural parameters

The structural parameters in the first group are the starting point of the construction, as they characterise a family of models defined as a set of systems sharing the same dimensionless density distribution $\tilde{\varrho}_{*i}$, while varying the specific values of the mass weights and the kinematical decomposition parameters.

The system analysed in this work includes two components, with a stellar density distribution described by the general $\mathrm{R}^{1/n}$ profile (see Sec. 2.2). Therefore, to define the scaled density components $\tilde{\varrho}_{*i}$, it is necessary to specify the Sérsic indices n_i that describe the density profile shapes (or, more generally, other parameters for different profile types), the shape parameters q_i, i.e. the flattenings in the case of ellipsoidal density distributions, and the scale-length ratios $x_i = r_{*i}/r_*$.

The values of the structural parameters must be assigned prior to running the P&JS module, because, in general, any change in these parameters requires a recomputation of both the gravitational potentials and the solutions of the Jeans equations.

3.3.2 Weights

In the original code `JASMINE2` (Caravita 2022), the second group of parameters comprises the relative mass weights $R_i \equiv M_{*i}/M_*$ and the mass-to-light ratios $\Upsilon_{*i} \equiv M_{*i}/L_{*i}$. For the present work, it was natural to fix the known luminosities L_i, so that, for chosen mass-to-light ratios Υ_{*i}, the corresponding stellar mass weights R_i can be derived.

Considering that by definition the sum of all relative mass weights is normalised to unity ($\sum_i R_i = 1$), the weights can then be applied to the scaled, dimensionless quantities produced by the P&JS module, leading to the following expression for the stellar components

$$\varrho_{*i} = \varrho_n R_i \tilde{\varrho}_{*i}, \tag{3.5}$$

The total stellar density can therefore be written as

$$\varrho_* = \varrho_n \tilde{\varrho}_* = \varrho_n \sum_i R_i \tilde{\varrho}_{*i}, \tag{3.6}$$

where $\tilde{\varrho}_{*i}$ denotes the dimensionless density distributions of the stellar components, while $\tilde{\varrho}_*$ represents the dimensionless total stellar density, obtained by weighting each component according to its relative mass fraction.

From the assumption of a constant mass-to-light ratio Υ_{*i} for each stellar component, the corresponding luminosity density can be written as

$$\nu_{*i} = \varrho_n \frac{R_i}{\Upsilon_{*i}} \tilde{\varrho}_{*i}, \tag{3.7}$$

so that the luminosity density follows the shape of the scaled mass density $\tilde{\varrho}_{*i}$.

The values of the weights are assigned during the PP stage, since variations in their values or in the adopted kinematical decompositions do not require recomputing the gravitational potentials or solving the Jeans equations again. This approach makes the PP phase more flexible and computationally efficient, allowing different combinations of parameters to be explored. In this way, starting from a fixed set of structural parameters, one can generate an entire family of models that share the same dimensionless density distribution but differ in their relative mass contributions and dynamical configurations, thereby enabling the identification of the parameters combinations that best reproduce the observed photometric and kinematic properties.

3.3.3 Physical scales

The third group of model parameters includes the physical scales M_*, the total stellar mass, and a chosen scale length for the system r_*.

All masses and lengths are normalised to M_* and r_*, respectively. The numerical grid is also normalised to r_*, so that the scaled grid $(\tilde{R}, \tilde{z})$, with $\tilde{R} \equiv R/r_*$ and $\tilde{z} \equiv z/r_*$, ensures the same spatial resolution independently of the actual physical size of the model, measured by r_*.

All density and potential components are made dimensionless by scaling them, respectively, with the normalisation coefficients

$$\varrho_n \equiv \frac{M_*}{4\pi r_*^3}, \qquad \phi_n \equiv \frac{GM_*}{r_*}. \tag{3.8}$$

Even though the physical scales are logically introduced first, the values of M_* and r_* (and the derived normalisation ϱ_n and ϕ_n) are fixed at the last step of the model construction. In this way, different physical realisations (in total mass and size) can be obtained for the same multicomponent galaxy model.

Although the physical scales are logically introduced first, e.g. in the normalisation of the grid of the numerical code, the values of M_* and r_* (and the derived normalisations ϱ_n and ϕ_n) are fixed at the final stage of the model construction. In this way, the code flexibility allows the exploration of a wide range of physical configurations within the same family of models, since different physical realisations (in total mass and size) can be obtained for the same multicomponent galaxy model.

3.4 Potential & Jeans Solver

For N chosen sets of values for the structural parameters, describing N assigned scaled stellar densities $\tilde{\varrho}_{*i}$, for the purposes of this work, the P&JS computes the N scaled gravitational potentials $\tilde{\phi}_j$, and then solves the $N \times N$ systems of scaled Jeans equations, one for each $\tilde{\varrho}_{*i}$ within each potential $\tilde{\phi}_j$.

The P&JS operates on three axisymmetric grids in $(\tilde{R}, \tilde{z})$: a principal grid, on which all quantities are calculated, and two auxiliary grids used to evaluate derivatives through a centred finite-difference numerical approximation.

The adopted grid is slightly logarithmic and extends from 5×10^{-3} to 80 (in r_* units), with a total of 350 points.

3.4.1 N systems of Jeans equations

Although the code is able to accommodate more general distribution functions, including three-integral distribution functions, in this work each stellar component is assumed to be described by a two-integral distribution function $f_i(E, J_z)$, where E and J_z denote, respectively, the energy and the axial component of the angular momentum per unit mass of each star in the total potential Φ. This choice is consistent with the modelling strategy adopted for the two axisymmetric components considered here.

For axisymmetric systems, under the assumption of two-integral distribution functions and adopting cylindrical coordinates, the velocity moments of each stellar component satisfy the following relations (Binney et al. 2008):

$$\overline{v_{Ri}} = \overline{v_{zi}} = 0, \tag{3.9}$$

$$\overline{v_R v_{zi}} = \overline{v_z v_{\phi_i}} = \overline{v_R v_{\phi_i}} = 0, \qquad \overline{v_{Ri}^2} = \overline{v_{zi}^2}, \tag{3.10}$$

$$\sigma_{Ri}^2 = \sigma_{zi}^2 \equiv \sigma_i^2. \tag{3.11}$$

The dynamical state of the galaxy composed by N stellar components is determined by N systems of Jeans equations

$$\begin{cases} \dfrac{\partial(\varrho_{*i}\sigma_i^2)}{\partial z} = -\varrho_{*i}\dfrac{\partial \Phi}{\partial z}, \\ \dfrac{\partial(\varrho_{*i}\sigma_i^2)}{\partial R} = \varrho_{*i}\dfrac{\Delta_i}{R} - \varrho_{*i}\dfrac{\partial \Phi}{\partial R}, \end{cases} \tag{3.12}$$

which relate the total gravitational potential Φ to the velocity moments of each stellar component, considering the following definition

$$\Delta_i \equiv \overline{v_{\phi_i}^2} - \sigma_i^2, \qquad \sigma_{\phi i}^2 = \overline{v_{\phi_i}^2} - \overline{v_{\phi_i}}^2 = \Delta_i + \sigma_i^2 - \overline{v_{\phi_i}}^2. \tag{3.13}$$

The equations expressed here in their theoretical form are translated through the `JASMINE2` code into a discretised system over a spatial grid and the derivatives are computed by centred numerical differentiation methods.

3.4.2 N × N systems of Jeans equations

The properties of the Poisson and the Jeans equations allow scaling operations, making it possible to compute a set of scaled, i.e., dimensionless, solutions.

In particular, the Jeans equations (3.12), for a fixed total potential Φ, are invariant under a mass scaling of the density ϱ_{*i}. This means that, at fixed Φ, the derived velocity fields are independent of the specific value of M_{*i}. The Jeans equations (3.12) can be decomposed according to the contribution of each potential component ϕ_j, recalling that $\Phi = \sum_j \phi_j$, leading to $N \times N$ systems of equations for the N stellar densities ϱ_{*i} in the N potentials ϕ_j

$$\begin{cases} \dfrac{\partial(\varrho_{*i}\sigma_{ij}^2)}{\partial z} = -\varrho_{*i}\dfrac{\partial \phi_j}{\partial z}, \\ \dfrac{\partial(\varrho_{*i}\sigma_{ij}^2)}{\partial R} = \varrho_{*i}\dfrac{\Delta_{ij}}{R} - \varrho_{*i}\dfrac{\partial \phi_j}{\partial R}, \end{cases} \tag{3.14}$$

where the double subscript ij labels the solution of the i-th stellar component within the j-th potential component.

The solutions to the systems (3.14) are

$$\varrho_{*i}\sigma_{ij}^2 = \int_z^\infty \varrho_{*i}\frac{\partial \phi_j}{\partial z'}\mathrm{d}z', \qquad \varrho_{*i}\Delta_{ij} = R\left(\frac{\partial \varrho_{*i}\sigma_{ij}^2}{\partial R} + \varrho_{*i}\frac{\partial \phi_j}{\partial R}\right), \tag{3.15}$$

with $\varrho_{*i}\sigma_{ij}^2 \to 0$ for $z \to \infty$.

It is worth noting that the ability to solve the systems of Jeans equations without specifying the relative mass ratios arises from the fact that, on the one hand, the weights appear linearly on both sides of the equations and, on the other hand, once the boundary condition is fixed to zero at infinity, the quantities $\tilde{\sigma}_{ij}^2$ and $\tilde{\Delta}_{ij}$ scale linearly with the mass ratios.

3.5 Post Processing

The PP stage operates on the scaled solutions $\tilde{\sigma}_{ij}^2$ and $\tilde{\Delta}_{ij}$ computed by the P&JS for a given multicomponent model, working on the same slightly logarithmic grid of the P&JS module.

The solutions are combined through the assignment of mass ratios R_j, yielding the solutions $\tilde{\sigma}_i^2$ and $\tilde{\Delta}_i$.

In order to proceed with the kinematical decomposition of the azimuthal motion, a positivity check is performed on $\tilde{\Delta}_{ij}$ (for the Satoh k-decomposition) and $\tilde{\Delta}_i + \tilde{\sigma}_i^2$ (for

the generalised k-decomposition), in a way that limiting values on the weights R_j are constrained, discarding models that cannot satisfy physical meaningfulness.

The adopted kinematical decomposition is chosen and specified via the parameters k_i, which determine the normalised azimuthal velocity fields $\tilde{v}_{\phi i}$.

In this module, the projections along a given line of sight are performed, using the standard trapezoidal rule. Given that all the projection formulae are linearly proportional to all the weights, except the line-of-sight rotational velocity $v_{\rm los}$, it is worth noting that all the scaled projected fields are calculated in a first step of the code, while $v_{\rm los}$ is computed separately after the choice of the mass weights, in a way that a change in the weights does not require to compute again all the projections.

In this work, additional routines have been developed to complete the construction of the physical model from the scaled outputs of the PP module implemented by Caravita (2022). First, each projected quantity is considered with its relative contribution R_i, through a dedicated block of code designed to handle this weighting procedure in a systematic way.

Furthermore, the routines allow both the implementation of different functional forms and the variation of the weights for the kinematical parameters, enabling the exploration of different azimuthal velocity configurations within the same set of scaled solutions.

Subsequently, a further module assigns the values of the total stellar mass M_* and the characteristic scale-length r_*. This routine performs the final conversion from dimensionless to physical units, ensuring that the internal structure, dynamics and the relative contributions in mass and luminosity of the different components remain unchanged.

Through these additional routines, the PP stage is extended so as to generate a complete family of physical models from a single set of dimensionless and scaled solutions, allowing variations in mass contributions, kinematical configurations, and finally in the physical scales of the system.

3.5.1 Weighting

According to what was discussed in Subsec. 3.3.2, the ij-th solution of the Jeans equations (3.15) can be written as

$$\sigma_{ij}^2 = \phi_n R_j \tilde{\sigma}_{ij}^2, \qquad \Delta_{ij} = \phi_n R_j \tilde{\Delta}_{ij}. \tag{3.16}$$

Consequently the i-th solutions, σ_i^2 and Δ_i, are obtained by summing over all j

$$\sigma_i^2 = \phi_n \tilde{\sigma}_i^2 = \phi_n \sum_j R_j \tilde{\sigma}_{ij}^2, \qquad \Delta_i = \phi_n \tilde{\Delta}_i = \phi_n \sum_j R_j \tilde{\Delta}_{ij}. \tag{3.17}$$

Hence, the total solutions σ^2 and Δ are derived by summing over i, including the normalisation of the stellar density distributions.

Since $\bar{v}_{\phi i}$ and $\sigma^2_{\phi i}$ are determined by σ^2_i and Δ_i, their scaling after the projection procedure directly follows from the preceding equations. In addition, the parameters k_i, governing the decomposition of the azimuthal motions according to (3.19)–(3.20), are incorporated in the sums over i.

3.5.2 Azimuthal velocity decomposition

A critical aspect of the modelling is the decomposition in random and ordered motion of the azimuthal component of the second order velocity moment $\overline{v^2_{\phi_i}}$, since in the specific case of axisymmetric systems in principle $\overline{v_{\phi_i}} \neq 0$ and it is essential for capturing rotation.

The Jeans equations (3.12) are degenerate in the azimuthal direction, since the kinematical fields solutions do not put any constraint on the first order velocity moment $\overline{v_{\phi_i}}$. There is freedom in choosing the streaming velocity field, i.e the systematic average rotation around the symmetry axis, with the only constraint given by the definition

$$\overline{v^2_{\phi_i}} = \sigma^2_{\phi i} + \overline{v_{\phi_i}}^2, \tag{3.18}$$

In multicomponent systems such as galaxies each population can have distinct rotational properties, necessitating a theoretical framework to separate random motions from ordered rotation. The N systems approach (Subsec. 3.4.1) ensures that each stellar component can have its own anisotropy profile, reflecting realistic differences in orbital structure.

The `JASMINE2` code implements the decomposition of the azimuthal motion, allowing to choose between two different prescriptions for $\overline{v_\phi}$.

Satoh k-decomposition

The Satoh k-decomposition (Satoh 1980), valid for systems with $\Delta_i \geq 0$, expresses the streaming velocity of each stellar component as

$$\overline{v_{\phi_i}} = k_i \sqrt{\Delta_i} \tag{3.19}$$

and then it follows

$$\sigma^2_{\phi i} = \sigma^2_i + (1 - k_i^2)\Delta_i, \tag{3.20}$$

with $k_i^2 \leq 1$ and negative values of k_i describing clockwise rotation.

The parameter $k_i = 0$ describes systems with no net rotation ($\overline{v_{\phi_i}} = 0$), while $k_i^2 = 1$ describes the isotropic rotator case, with a isotropic velocity dispersion tensor ($\sigma^2_{\phi i} = \sigma^2_i$).

In the simpler kinematical decomposition, k_i is assumed constant over the whole space; more general decompositions can be obtained by adopting a position-dependent parameter $k_i(R, z)$.

Actually, the true upper limit on k_i^2 is given by the physical condition $\overline{v_{\phi i}}^2 \leq \overline{v_{\phi_i}^2}$. In particular, k_i^2 is maximum when the two terms are equal, so it follows

$$k_i^2 \Delta_i = \overline{v_{\phi i}}^2, \qquad k_i^2 = \frac{\overline{v_{\phi i}}^2}{\Delta_i}, \tag{3.21}$$

that more explicitly, using the definition in (3.13), yields

$$k_i^2 = 1 + \frac{\sigma_i^2}{\Delta_i}. \tag{3.22}$$

The k parameter

In the numerical implementation, the decomposition parameter of each stellar component k_i is defined as

$$k_i(R, z) = \lambda_i \delta_i(R, z) \tag{3.23}$$

where λ_i is a constant weight and $\delta_i(R, z)$ is a position-dependent function. The factorisation of the k_i parameter in two sub-parameters allows to set the value of the constant weight λ_i after the projection integrals, since the integration of $\tilde{v}_{\phi i}$ scales with λ_i, for fixed $\delta_i(R, z)$.

Using this generalisation, cases of rotating systems with a spatially-dependent k parameter can be explored, implementing (as done extending the `JASMINE2` routines) functions as

$$k_a(r) = k_0 + (k_\infty - k_0)\frac{\tilde{R}}{\xi_0 + \tilde{R}}, \qquad k_e(r) = \mathrm{e}^{-r/\langle R_e \rangle}, \tag{3.24}$$

where k_0 and k_∞ are respectively the central value of the k parameter and its value at infinity, $\langle R_e \rangle = \sqrt{q_*} R_e$ is the circularised effective radius of an ellipsoidal stellar system observed edge-on (Ciotti et al. 2022). Using the $k_a(r)$ expression, in the outskirts $\overline{v_\phi}$ becomes asymptotically flat, while in the central region $k_a(0) = k_0$; in the exponential case, $\overline{v_\phi}$ decreases significantly at large radii, while in the central region stars rotate almost as fast as in the isotropic rotator case (Fig. 3.2).

3.5.3 Projections

Projection translates intrinsic three-dimensional quantities into observables on the plane of the sky. The numerical code `JASMINE2` incorporates a projection framework that allows the generation of observable maps by integrating along the line of sight, treating each component independently and combining them only afterward according to the chosen weighting schemes. On this basis, in this Section the subscript i is omitted, but the following reasoning applies separately to each stellar density component ϱ_{*i} as well as to the total density ϱ_*.

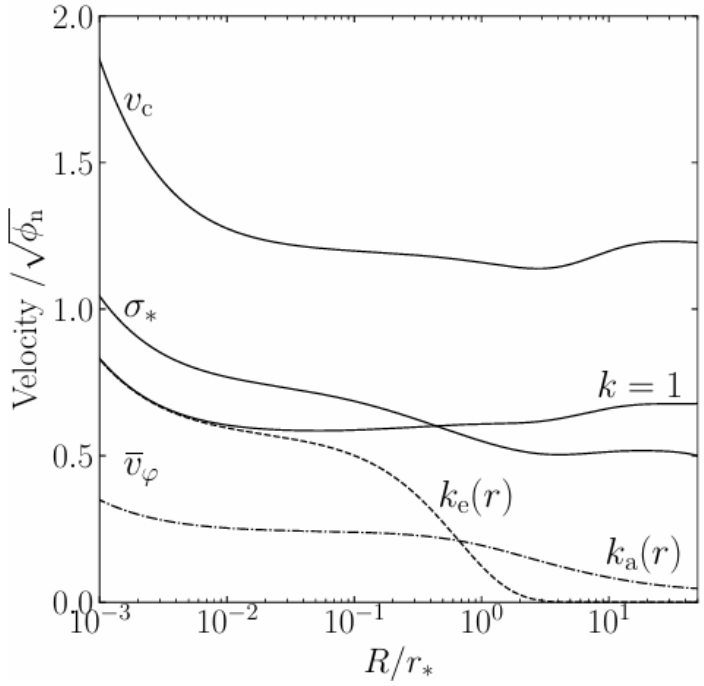

Figure 3.2: Radial profiles of the stellar velocities in the equatorial plane in units of $\sqrt{\phi_n}$ (effect of a central SMBH included), showing different position-dependent functions $k(R, z)$: circular velocity v_c, stellar vertical velocity dispersion component σ_*, and the three different azimuthal streaming velocities $\overline{v_\phi}$, respectively for the isotropic rotator (solid line, $k = 1$), for the exponentially declining Satoh decomposition (dashed line, $k = k_e$), and asymptotically flat Satoh decomposition (dot-dashed line, $k = k_a$). Taken from Ciotti et al. (2022).

The projection formulae from Caravita (2022) and Posacki (2014) hold for a generic inclination of the line of sight with respect to the galaxy. For axisymmetric models, here it is assumed without loss of generality that the line of sight is parallel to the $x-z$ plane, and the projection plane rotates around the y axis.

The projections of the stellar density and of the ordered velocity $\mathbf{v} = \bar{v}_\phi \mathbf{e}_\phi$ are

$$\Sigma_* = \int_{-\infty}^{\infty} \varrho_* \mathrm{d}l, \qquad \Sigma_* = \int_{-\infty}^{\infty} \varrho_* \bar{v}_\phi < \mathbf{e}_\phi, \mathbf{n} > \mathrm{d}l, \tag{3.25}$$

where l is the integration path along the line of sight, in the direction $\mathbf{n}$, directed from the observer to the galaxy; $\mathbf{e}_\phi = (-\sin\phi, \cos\phi, 0)$ is the unitary vector in the tangential direction .

The line-of-sight velocity dispersion can be written as

$$\sigma_{\mathrm{los}}^2 = \sigma_{\mathrm{P}}^2 + V_{\mathrm{P}}^2 - v_{\mathrm{los}}^2 = V_{\mathrm{rms}}^2 - v_{\mathrm{los}}^2, \tag{3.26}$$

accordingly to the definition from Cappellari (2008)

$$V_{\mathrm{rms}}^2 \equiv \sigma_{\mathrm{P}}^2 + V_{\mathrm{P}}^2 = \sigma_{\mathrm{los}}^2 + v_{\mathrm{los}}^2, \tag{3.27}$$

where V_{P}^2 is the projection of the square of the component along $\mathbf{n}$ of the ordered velocity, and σ_{P}^2 is the projected velocity dispersion. Note that σ_{P}^2 is not the line-of-sight (i.e. the observed) velocity dispersion if a net rotation is present (Ciotti et al. 1996).

More in details, the projections of these quantities are

$$\Sigma_* \sigma_{\mathrm{P}}^2 = \int_{-\infty}^{\infty} \varrho_* < \mathbf{s}^2 \mathbf{n}, \mathbf{n} > \mathrm{d}l, \qquad \Sigma_* V_{\mathrm{P}}^2 = \int_{-\infty}^{\infty} \varrho_* \bar{v}_\phi^2 < \mathbf{e}_\phi, \mathbf{n} >^2 \mathrm{d}l, \tag{3.28}$$

where σ is the 3×3 velocity dispersion tensor.

In the specific case of edge-on projection, the line of sight is aligned with the x axis with $\mathbf{n} = -\mathbf{e}_x$, so that the projection plane coincides with the $y - z$ plane, and $(\cos\phi, \sin\phi) = (x/R, y/R)$, where $R = \sqrt{x^2 + y^2}$. Therefore the following projection formulae follow.

From the integrals (3.28) it is possible to derive

$$\Sigma_* \sigma_{\mathrm{P}}^2 = 2 \int_y^{\infty} \frac{(R^2 - y^2)\sigma^2 + y^2 \sigma_\phi^2}{R\sqrt{R^2 - y^2}} \varrho_* \mathrm{d}R, \tag{3.29}$$

$$\Sigma_* V_{\mathrm{P}}^2 = 2y^2 \int_y^{\infty} \frac{\varrho_* \overline{v_\phi}^2}{R\sqrt{R^2 - y^2}} \mathrm{d}R, \tag{3.30}$$

and then, in a more compact form, exploiting the definition (3.13) in Eq. (3.26)

$$\Sigma_* \sigma_{\mathrm{los}}^2 = 2 \int_y^{\infty} \frac{R^2 \sigma^2 + y^2 \Delta}{R\sqrt{R^2 - y^2}} \varrho_* \mathrm{d}R - \Sigma_* v_{\mathrm{los}}^2. \tag{3.31}$$

Mass-weighted and luminosity-weighted projections

The mass-weighted and luminosity-weighted projected quantities, given that the projection integrals are already computed by the standard `JASMINE2` projection routines, are jointly handled in a dedicated module developed specifically for this work. This includes the numerical implementation of equations (3.32)–(3.33) to combine the pre-computed projections according to the adopted component weights.

Mass-weighted projections emphasise the contribution of each point along the line of sight according to local mass density, $\varrho_{*i}(R, z)$.

The projected properties of a multicomponent stellar system can be obtained by considering the sums:

$$\Sigma_* = \sum_i \Sigma_{*i}, \qquad v_{\rm los} = \frac{\sum_i \Sigma_{*i} v_{{\rm los}i}}{\Sigma_*}, \qquad V^2_{\rm rms} = \frac{\sum_i \Sigma_{*i} V^2_{{\rm rms}i}}{\Sigma_*}, \tag{3.32}$$

and $\sigma^2_{\rm los}$ is given by (3.26).

Luminosity-weighted projections account for the observed light distribution, weighting contributions by the local luminosity density $\nu_{*i}(R, z)$, producing observables that can be directly compared to spectroscopic or photometric measurements.

`JASMINE2` allows the implementation of different constant mass-to-light ratios Υ_{*i} for each stellar component. In analogy to (3.32), the luminosity-weighted fields are defined by using the surface brightness distribution

$$I_{*i} = \frac{\Sigma_{*i}}{\Upsilon_{*i}}, \qquad I_* = \sum_i I_{*i}, \tag{3.33}$$

in lieu of the surface densities Σ_{*i} and Σ_*.

3.5.4 Physical dimensions

The routine responsible for combining and converting scaled quantities into physical ones, incorporating the introduction of M_*, r_*, and the rescaling of all projected fields, has been implemented as part of this study.

The physical quantities needed for the description of the multicomponent system, for the N components and for the total density distribution, are recovered as weighted sums of the scaled and normalised solutions, output of the PP module: $\tilde{\Sigma}_{*i}$, $\tilde{\Sigma}_{*i}\tilde{v}_{{\rm los}i}$, $\tilde{\Sigma}_{*i}\tilde{V}^2_{{\rm P}ij}$, and $\tilde{\Sigma}_{*i}\tilde{\sigma}^2_{{\rm P}ij}$.

The projected surface density distribution Σ_* is obtained from $\tilde{\Sigma}_{*i}$ as

$$\Sigma_{*i} = R_i \tilde{\Sigma}_{*i} \varrho_n r_*, \qquad \Sigma_* = \sum_i \Sigma_{*i}. \tag{3.34}$$

The projected mass-weighted rotational velocity $v_{\rm los}$ is obtained from $\tilde{\Sigma}_{*i}\tilde{v}_{{\rm los}i}$ as

$$\Sigma_{*i}v_{{\rm los}i} = \lambda_i\tilde{\Sigma}_{*i}\tilde{v}_{{\rm los}i}\sqrt{\phi_n}, \qquad v_{{\rm los}i} = \frac{\Sigma_{*i}v_{{\rm los}i}}{\Sigma_{*i}}, \qquad v_{\rm los} = \sum_i \frac{\Sigma_{*i}v_{{\rm los}i}}{\Sigma_*}. \tag{3.35}$$

Notice that the solutions $\tilde{\Sigma}_{*i}\tilde{v}_{{\rm los}i}$ include the R_i, R_j contributions (as discussed in Sec. 3.5).

The projected mass-weighted velocity dispersion $\sigma_{\rm los}$ is obtained from $\tilde{\Sigma}_{*i}\tilde{V}^2_{{\rm P}ij}$ and $\tilde{\Sigma}_{*i}\tilde{\sigma}^2_{{\rm P}ij}$, using (3.26) and (3.27), as

$$\tilde{\Sigma}_{*i}\tilde{V}^2_{{\rm P}i} = \sum_j [R_j(\tilde{\Sigma}_{*i}\tilde{V}^2_{{\rm P}ij})], \qquad \Sigma_{*i}V^2_{{\rm P}i} = R_i\tilde{\Sigma}_{*i}\tilde{V}^2_{{\rm P}i}\sqrt{\phi_n}, \qquad \Sigma_*V^2_{\rm P} = \sum_i \Sigma_{*i}V^2_{{\rm P}i}, \tag{3.36}$$

$$\tilde{\Sigma}_{*i}\tilde{\sigma}^2_{{\rm P}i} = \sum_j [R_j(\tilde{\Sigma}_{*i}\tilde{\sigma}^2_{{\rm P}ij})], \qquad \Sigma_{*i}\sigma^2_{{\rm P}i} = R_i\tilde{\Sigma}_{*i}\tilde{\sigma}^2_{{\rm P}i}\sqrt{\phi_n}, \qquad \Sigma_*\sigma^2_{\rm P} = \sum_i \Sigma_{*i}\sigma^2_{{\rm P}i}, \tag{3.37}$$

therefore, for each stellar component

$$\Sigma_{*i}V^2_{{\rm rms}i} = \Sigma_{*i}V^2_{{\rm P}i} + \Sigma_{*i}\sigma^2_{{\rm P}i}, \qquad \sigma_{{\rm los}i} = \sqrt{\frac{\Sigma_{*i}V^2_{{\rm rms}i}}{\Sigma_{*i}} - v^2_{{\rm los}i}}; \tag{3.38}$$

and for the total

$$\Sigma_*V^2_{\rm rms} = \Sigma_*V^2_{\rm P} + \Sigma_*\sigma^2_{\rm P}, \qquad \sigma_{\rm los} = \sqrt{\frac{\Sigma_*V^2_{\rm rms}}{\Sigma_*} - v^2_{\rm los}}. \tag{3.39}$$

Similarly, the luminosity-weighted quantities are obtained from the same solutions in output from the P&JS, using the prescription in (3.33).

The projected surface brightness distribution I_* is obtained from $\tilde{\Sigma}_{*i}$ as

$$I_{*i} = R_i\frac{\tilde{\Sigma}_{*i}}{\Upsilon_{*i}}\varrho_n r_*, \qquad I_* = \sum_i I_{*i}. \tag{3.40}$$

The projected luminosity-weighted rotational velocity $v_{{\rm los},\ell}$ is obtained from $\tilde{\Sigma}_{*i}\tilde{v}_{{\rm los}i}$ as

$$I_{*i}v_{{\rm los}i} = \lambda_i\frac{\tilde{\Sigma}_{*i}\tilde{v}_{{\rm los}i}}{\Upsilon_{*i}}\sqrt{\phi_n}, \qquad v_{{\rm los},\ell} = \sum_i \frac{I_{*i}v_{{\rm los}i}}{I_*}. \tag{3.41}$$

The projected luminosity-weighted velocity dispersion $\sigma_{{\rm los},\ell}$ is obtained from $\tilde{\Sigma}_{*i}\tilde{V}^2_{{\rm P}ij}$ and $\tilde{\Sigma}_{*i}\tilde{\sigma}^2_{{\rm P}ij}$ as

$$\tilde{\Sigma}_{*i}\tilde{V}^2_{\mathrm{P}i} = \sum_j [R_j(\tilde{\Sigma}_{*i}\tilde{V}^2_{\mathrm{P}ij})], \qquad I_{*i}V^2_{\mathrm{P}i} = R_i \frac{\tilde{\Sigma}_{*i}\tilde{V}^2_{\mathrm{P}i}}{\Upsilon_{*i}}\sqrt{\phi_n}, \qquad I_*V^2_{\mathrm{P}} = \sum_i I_{*i}V^2_{\mathrm{P}i}, \quad (3.42)$$

$$\tilde{\Sigma}_{*i}\tilde{\sigma}^2_{\mathrm{P}i} = \sum_j [R_j(\tilde{\Sigma}_{*i}\tilde{\sigma}^2_{\mathrm{P}ij})], \qquad I_{*i}\sigma^2_{\mathrm{P}i} = R_i \frac{\tilde{\Sigma}_{*i}\tilde{\sigma}^2_{\mathrm{P}i}}{\Upsilon_{*i}}\sqrt{\phi_n}, \qquad I_*\sigma^2_{\mathrm{P}} = \sum_i I_{*i}\sigma^2_{\mathrm{P}i}, \quad (3.43)$$

therefore, for the total stellar system

$$I_*V^2_{\mathrm{rms}} = I_*V^2_{\mathrm{P}} + I_*\sigma^2_{\mathrm{P}}, \qquad \sigma_{\mathrm{los},\ell} = \sqrt{\frac{I_*V^2_{\mathrm{rms}}}{I_*} - v^2_{\mathrm{los},\ell}}. \quad (3.44)$$

Note that, under the assumption of a constant mass-to-light ratio Υ_{*i}, the mass scales linearly with the luminosity, so the luminosity-weighted and mass-weighted maps of each component are identical.

Chapter 4

The two-component models

This chapter presents the construction and exploration of dynamical models composed of two axisymmetric stellar components. While the general structure and numerical framework follow the methods introduced in Chap. 3, the present discussion focuses on the specific parameter choices, weighting schemes, and post-processing procedures adopted for the case study of NGC 1366. Particular attention is devoted to the treatment of the free parameters and to the role of the post-processing stage (PP), where the family of models is generated and the numerical routines developed for this work are applied.

Sec. 4.1 summarises the setup of the Potential & Jeans Solver (P&JS) for the two-component configuration, describing the construction of the family of models.

Sec. 4.2 illustrates the Post-Processing stage for the case study of NGC 1366, where individual physical models are constructed from the scaled P&JS solutions. The mass fractions are assigned, the kinematical decomposition is performed, and the projected observables are obtained.

The modelling procedure is tested through a series of diagnostic tests designed to understand the effects of free parameters variation.

Finally, Sec. 4.3 presents the comparison between the model predictions for $v_{\rm los}$ and $\sigma_{\rm los}$ with the same curves obtained from the observational data (M17), with the aim of assessing whether the two-component model can successfully reproduce the observed kinematics of NGC 1366.

4.1 The Potential & Jeans Solver

The adopted zero-hypothesis aims to describe the observed internal structure and dynamics of the galaxy with the simplest possible model, which includes only the two stellar components revealed by the photometric decomposition (M08), described in Sec. 2.2.

One run of the P&JS produces the progenitor of a family of two-component galaxy models corresponding to $N = 2$ scaled stellar density components $\tilde{\varrho}_{*i}$. These two

Component	n_i	q_i	x_i
Bulge	1.5	0.80	1.00
Disc	1.0	0.41	8.30

Table 4.1: Structural parameters provided as input to the P&JS to define the scaled stellar densities $\tilde{\varrho}_{*,i}$ for each component in the two-component models: Sérsic indices n_i, intrinsic flattenings q_i and scale-length ratios x_i.

components describe the bulge and the disc of the modelled galaxy: a Sérsic stellar density distribution with Sérsic index $n_b = 1.5$ and flattening $q_b = 0.80$ to represent the bulge, and another Sérsic distribution with $n_d = 1$ and $q_d = 0.41$ to represent the exponential disc. The adopted values are directly taken from the photometric decomposition of M08, ensuring consistency with the observational data (see Sec. 2.2).

To easily implement the scaling of the two components, the scale-length ratio of the first component is set to

$$x_b = \frac{r_{*,b}}{r_*} = 1, \tag{4.1}$$

i.e. $r_* = r_{*,b}$, imposing in this way that the grid is normalised to the scale length of the bulge, in the Post-Processing explicitely chosen as $r_{*,b} = R_{e,b}$. This determines x_i of the second component as

$$x_d = \frac{r_{*,d}}{r_*} = \frac{R_{e,d}}{R_{e,b}} = 8.30, \tag{4.2}$$

from the ratio between the effective radii $R_{e,i}$ of bulge and disc. In particular, the disc effective radius $R_{e,d}$ (chosen as $r_{*,d}$) is obtained from the disc scale-length h (Sec. 2.2).

Therefore, the adopted grid which extends from 5×10^{-3} to 80 in r_* units (see Sec. 3.4), in physical scales covers from 10^{-3} to 17.04 kiloparsecs.

The structural parameters provided as input to the P&JS, which are required to define the scaled stellar densities $\tilde{\varrho}_{*,i}$, are listed in Tab. 4.1.

4.2 The Post-Processing

The second stage of the modelling, the Post-Processing, operates on the precise model progenitor constructed in the previous step, and produces a family of distinct models.

The mass fractions R_i are assigned as appropriate weights, in order to carry out the kinematical decomposition of the azimuthal velocity field in its ordered and random

components, to compute the projections along the line of sight and to sum the contributions of each i-th stellar component in all the j-th potential components. Until this step, in fact, the model produced by the `JASMINE2` code is independent of the stellar mass-to-light ratios Υ_{*i} and the mass fractions R_i.

In the specific case of NGC 1366, the photometric bulge–disc decomposition of M08 constrains the luminosities of the stellar components L_{*i} (see Sec. 2.2). Therefore, in the following analysis, the luminosities of the two stellar components are always kept fixed. Since the luminosities L_{*i}, the mass-to-light ratios Υ_{*i} and the mass fractions R_i are not three independent quantities, fixing the luminosities leaves only one free parameter for each component, among Υ_{*i} and R_i.

During the testing phase, the mass fractions R_i are prescribed, whereas when constructing the physical model for NGC 1366 it is preferred to vary the mass-to-light ratios Υ_{*i}. The Satoh parameters k_i, instead, remain free parameters both in the tests and in the galaxy model construction.

In the following discussion, the modelling procedure aims to assess whether a two-component model can reproduce the kinematic measurements along the major axis of NGC 1366 (retrieved from M17). An initial testing phase is devoted to exploring the effects of varying the free parameters, and the insights gained from this analysis are then employed to identify the model configuration that best describes the observational data.

4.2.1 Free parameters and their effects: tests

For the purpose of assessing the sensitivity of the dynamical solutions to variations in the free parameters, the tests are carried out on the same progenitor model generated in Sec. 4.1 (Tab. 4.1).

The tests are conducted by prescribing the mass fractions R_i, rather than the mass-to-light ratios Υ_{*i}, providing the total stellar mass of the system M_* and imposing constraining relations among the component masses M_{*i}.

This choice provides direct control over the construction of intentionally extreme configurations, enabling an examination of cases in which all the stellar mass resides in the disc, all in the bulge, or is equally distributed between the two components. These limiting scenarios, presented in Fig. 4.1, were implemented by imposing

$$M_{*,b} = 10^{-6} M_{*,d}, \qquad M_{*,d} = 10^{-6} M_{*,b}, \qquad M_{*,b} = M_{*,d}. \tag{4.3}$$

These conditions constrain the mass fractions R_i (as $M_{*i} = R_i M_*$), while the corresponding mass-to-light ratios follow straightforwardly for fixed total stellar mass M_*.

All tests are performed using the Satoh decomposition with a constant value of the parameter k_i for each component (Subsec. 3.5.2).

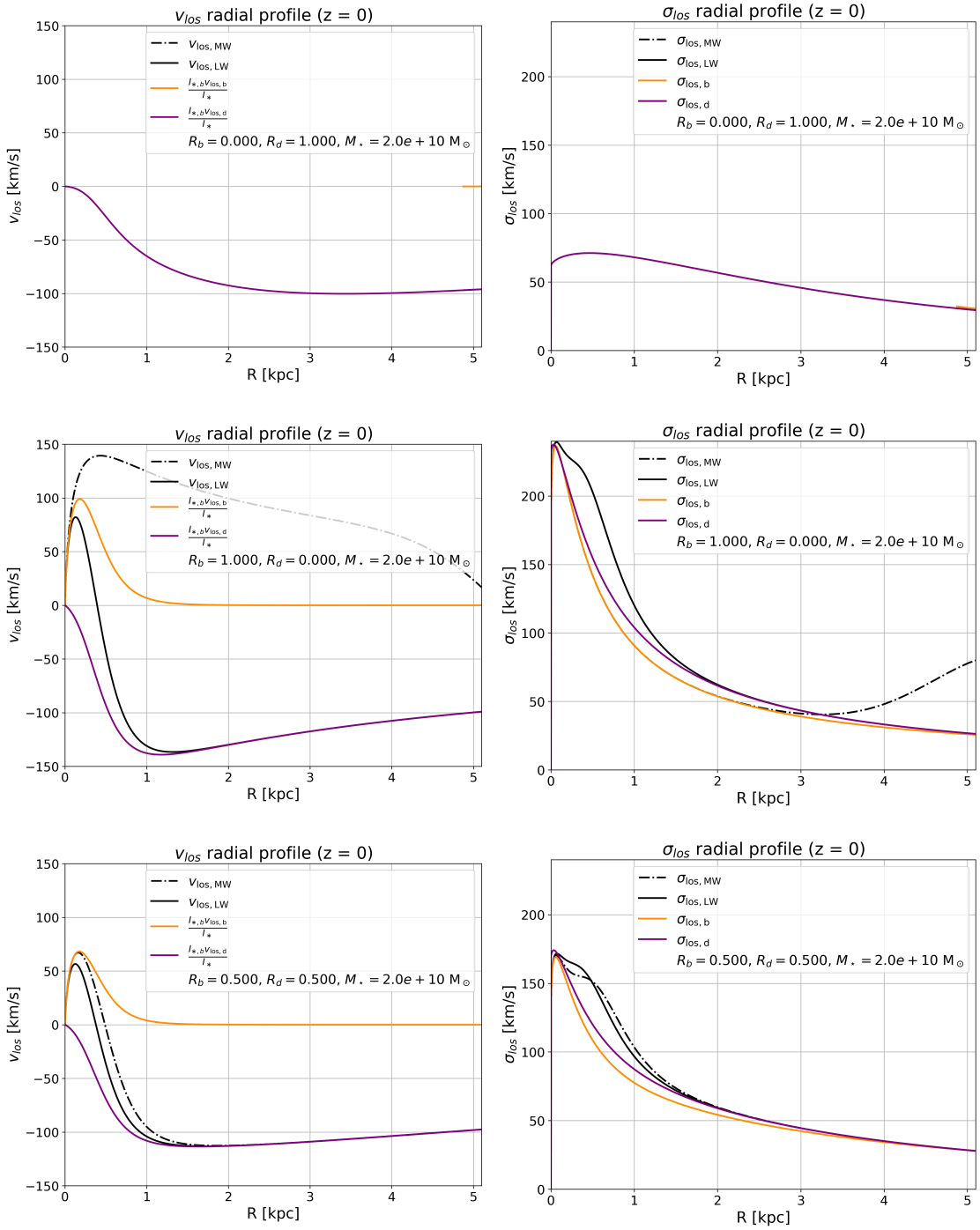

Figure 4.1: Stellar line-of-sight velocity profile $v_{\rm los}$ (*left column*) and velocity dispersion profile $\sigma_{\rm los}$ (*right column*) along the major axis, for two-component models with $M_* = 2 \times 10^{10}\,{\rm M}_\odot, k_i = \pm 1.0$ for the Satoh decomposition. Three different configurations are shown, corresponding to the extreme cases in Eq. 4.3: *top*: $R_b = 0.0$, $R_d = 1.0$ (note the problem relative to the lower limit on R_b discussed in the following subsection); *middle*: $R_b = 1.0$, $R_d = 0.0$; *bottom*: $R_b = 0.5$, $R_d = 0.5$.

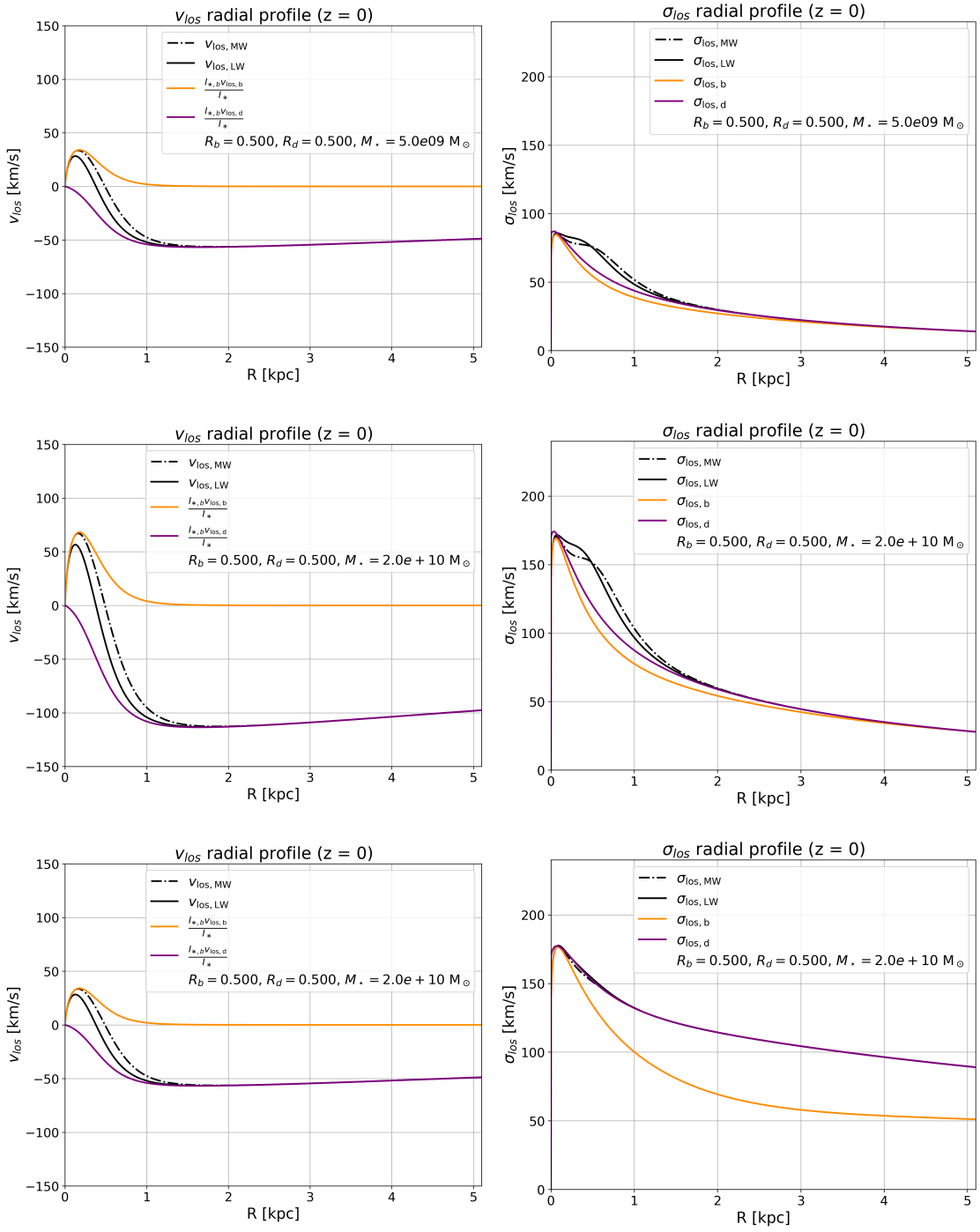

Figure 4.2: Stellar line-of-sight velocity profile $v_{\rm los}$ (*left column*) and velocity dispersion profile $\sigma_{\rm los}$ (*right column*) along the major axis, for two-component models with $R_b = R_d = 0.5$. Three different configurations are shown: *top*: $M_* = 5\times10^9\,{\rm M}_\odot$, $k_b = 1.0$, $k_d = -1.0$; *middle*: $M_* = 2\times10^{10}\,{\rm M}_\odot$, $k_b = 1.0$, $k_d = -1.0$; *bottom*: $M_* = 2\times10^{10}\,{\rm M}_\odot$, $k_b = 0.5$, $k_d = -0.5$, all for the Satoh decomposition.

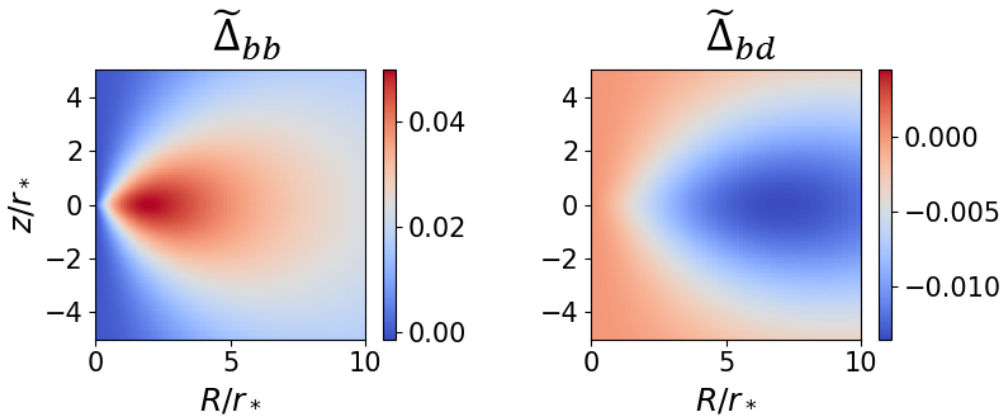

Figure 4.3: Two–dimensional maps in the $(\tilde{R}, \tilde{z})$ plane of the intrinsic quantities $\tilde{\Delta}_{bb}$ and $\tilde{\Delta}_{bd}$ (*bottom panels*), which are independent of the choice of R_i. The maps show that $\tilde{\Delta}_{bb}$ remains positive in the central region, while $\tilde{\Delta}_{bd}$ becomes somewhere negative, leading to a negative total $\tilde{\Delta}_b$ when the bulge mass fraction R_b is too small.

Lower limit on R_b

When recovering for the first time the rotation velocity $\overline{v}_{\phi,b}$ for the bulge, it is realised that a lower limit exists on R_b for the possibility of adopting the Satoh decomposition for azimuthal motions. This lower limit on the bulge mass fraction is $R_{b,\min} = 0.336$.

This threshold emerges while considering the maps of the $\tilde{\Delta}_{bb}$ and $\tilde{\Delta}_{bd}$ and their combination, needed to build Δ_b (Eq. 3.17). As shown in Fig. 4.4, $\tilde{\Delta}_b$ becomes somewhere negative for $R_b = 0.33$ and everywhere positive for $R_b = 0.34$.

To identify the origin of this behaviour, the intermediate quantities produced by the code are inspected, leading to the recognition that the problem arises from the quantity $\tilde{\Delta}_{bd}$, which is somewhere negative (Fig. 4.3). As a consequence, for the bulge component, $\tilde{\Delta}_b$ is found to become negative in the central regions of the galaxy.

From the Jeans equations under the two–component formalism, the quantity $\tilde{\Delta}_b$ can be written as a linear combination of the contributions associated with each pair of components (see Eq. 3.17):

$$\tilde{\Delta}_b = R_b\,\tilde{\Delta}_{bb} + R_d\,\tilde{\Delta}_{bd}, \tag{4.4}$$

where $\tilde{\Delta}_{bb}$ and $\tilde{\Delta}_{bd}$ depend solely on the structural properties of the model family (density distributions and gravitational potentials), while the mass fractions satisfy $R_d = 1 - R_b$.

Since $\tilde{\Delta}_{bb} > 0$ and $\tilde{\Delta}_{bd} < 0$ in the inner regions for models of this family (in Fig. 4.3), the condition $\tilde{\Delta}_b > 0$ imposes a constraint on the allowed values of R_b. The inequality

$$R_b\,\tilde{\Delta}_{bb} + (1 - R_b)\,\tilde{\Delta}_{bd} > 0 \tag{4.5}$$

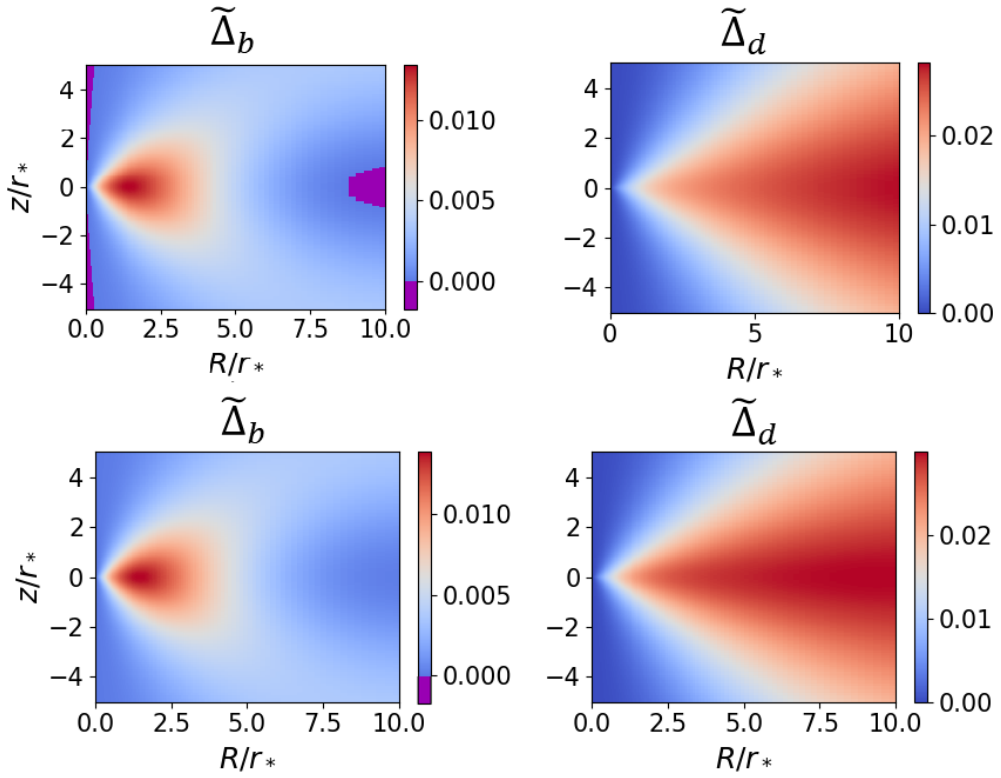

Figure 4.4: Two–dimensional maps in the $(\tilde{R}, \tilde{z})$ plane of the quantities $\tilde{\Delta}_b$ and $\tilde{\Delta}_d$, for different choices of R_i. *Top panels*: $R_b = 0.33$; *lower panels*: $R_b = 0.34$. Negative values are highlighted in purple.

can be solved explicitly, without exploring all the maps for each (R, z) value in all the different combinations with R_b, R_d, since it is sufficient to require:

$$R_b > -R_d \min\left(\frac{\tilde{\Delta}_{bd}}{\tilde{\Delta}_{bb}}\right), \tag{4.6}$$

yielding the strict lower bound on the bulge mass fraction:

$$R_b > R_{b,\min} = 0.336. \tag{4.7}$$

Thus, for $R_b < R_{b,\min}$, the Satoh decomposition cannot be consistently applied for the bulge, as the bulge would contribute too little mass to maintain the positivity of $\tilde{\Delta}_b$ in the central region. This restriction explains why in the "all-mass-in-the-disc" configuration it turns out that $\tilde{\Delta}_b < 0$ somewhere, as clear from Fig. 4.4 where a case with $R_b < R_{b,\min}$ (upper panels) is compared with a case with $R_b > R_{b,\min}$ (lower panels).

It is important to emphasise that the negativity of $\tilde{\Delta}_b$ arises solely from the intrinsic dynamical structure of the model, and that this constraint on R_b comes if one wants to adopt the Satoh decomposition. In particular, it does not depend on the choice of the PP parameters (such as the adopted values of the kinematical parameters k_i), which only determine how the permissible dynamical solutions are mapped into projected kinematic fields.

Bulge-dominated and disc-dominated kinematical regimes

As clear from Fig. 4.5, at small radii ($R \lesssim R_{e,b}$), the light distribution is dominated by the bulge and consequently the observed luminosity-weighted kinematics (modelled through the luminosity-weighted projected kinematical fields) in the central regions largely reflect the dynamical properties of the bulge component. Conversely, at large radii ($R \gtrsim 2$ kpc, i.e. well beyond the disc effective radius $R_{e,d}$), the surface brightness is dominated by the disc, whose contribution therefore drives the behaviour of the observed outer–region kinematics. The radius at which the bulge and disc surface brightness contributions are equal, $r_{db} = 5.0\,\mathrm{arcsec}$ (M08), corresponding to $r_{db} = 0.412\,\mathrm{kpc}$, marks a natural transition between these two regimes, and is clearly visible in Fig. 4.5.

Degeneracy between Υ_{*i} and k_i effects

The free parameters of the model construction for the galaxy NGC 1366 are the stellar mass-to-light ratios Υ_{*i} and the Satoh parameters k_i (as detailed in Sec. 4.2).

The testing procedure is designed to explore the interplay between these parameters, as both influence the predicted rotational support and velocity dispersion. An indication of the dependence of v_{los} (and consequently of σ_{los}) on these parameters can be inferred from the following considerations:

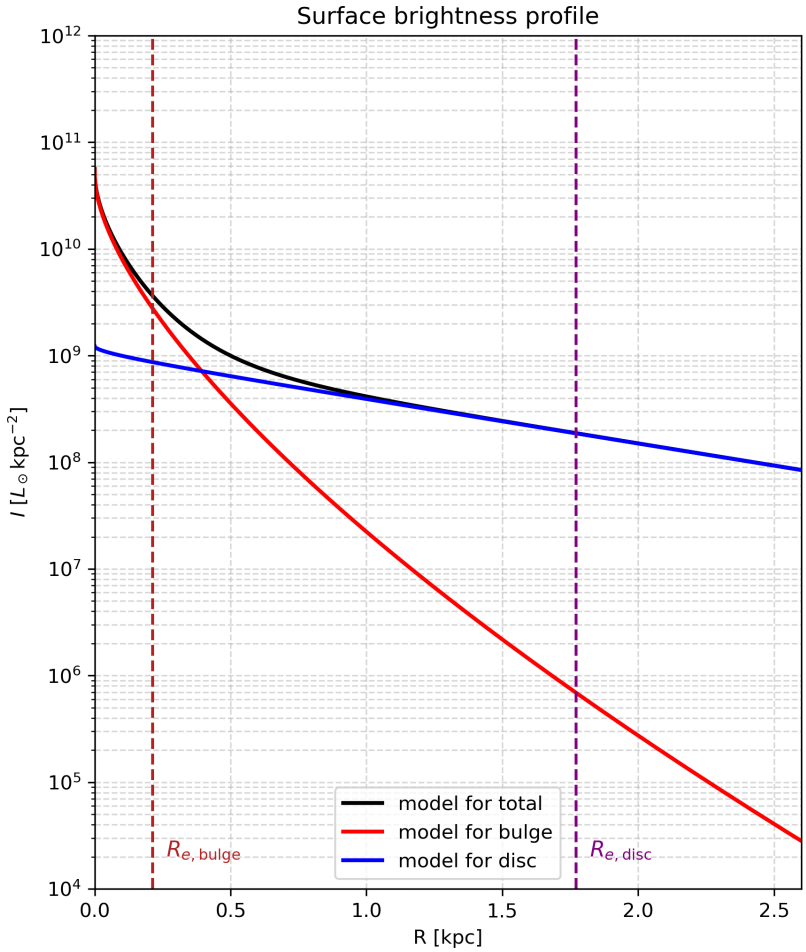

Figure 4.5: Two-component model for the radial profile of the surface brightness $I_*(R)$ of NGC 1366, showing the different contributions of the two components at different radii.

$$\bar{v}_{\phi i} = k_i \sqrt{\Delta_i}, \tag{4.8}$$

where, recalling $r_* = R_{e,b}$

$$\Delta_i \propto \phi_n = \frac{GM_*}{R_{e,b}} \qquad \text{and} \qquad M_* = \sum_i \Upsilon_{*i} L_{*i} \tag{4.9}$$

This reasoning shows that variations in either Υ_{*i} or k_i directly affect the intrinsic azimuthal velocity and, through projection, the observable line-of-sight velocity and velocity dispersion. Consequently, an increase in either parameter enhances the predicted rotational support, giving rise to a degeneracy: different combinations of Υ_{*i} and k_i can produce nearly identical v_{los} profiles.

In Fig. 4.2 (panels on the left), a reference model is selected (central panel), characterised by $(M_{*,\mathrm{ref}}, k_{i,\mathrm{ref}})$. Exploring the parameter space reveals that a model with lower stellar mass $(0.25M_{*,\mathrm{ref}}, k_{i,\mathrm{ref}})$ or with a lower Satoh parameter $(M_{*,\mathrm{ref}}, 0.5k_{i,\mathrm{ref}})$ produces an almost identical rotational velocity profile. This behaviour is fully consistent with the scaling relation $\bar{v}_{\phi i} \propto k_i\sqrt{M_*}$: reducing the total stellar mass by a factor of four lowers $\bar{v}_{\phi i}$ by a factor of two, which can be compensated either by maintaining the original k_i, or equivalently, keeping the mass fixed and reducing k_i by half. This explicitly illustrates the degeneracy between Υ_{*i} and k_i, showing that variations in these parameters can counterbalance each other to yield very similar observable line-of-sight kinematics.

4.2.2 Weighting scheme for the case study

If the mass-to-light ratios Υ_{*i} are specified, the mass fractions R_i can be derived in a straightforward way:

$$M_i = \Upsilon_{*i} L_i, \tag{4.10}$$

$$M_{\mathrm{tot}} = \sum_{i=1}^{N} M_i, \tag{4.11}$$

$$R_i = \frac{M_i}{M_{\mathrm{tot}}}. \tag{4.12}$$

In this way, the mass fractions R_i are determined after the choice of the mass-to-light ratios Υ_{*i} is made.

Estimates of the mass-to-light ratios Υ_{*i}

Representative mass-to-light ratios Υ_{*i} for the bulge and disc were obtained by using the photometric predictions based on the E-MILES SEDs (Vazdekis et al. 2012; Ricciardelli et al. 2012; Vazdekis et al. 2016), specifically the tables listing magnitudes, colours, and mass-to-light ratios in Johnson/Cousin filters (Vega system) computed with BaSTI isochrones for different Initial Mass Functions (IMF) (*E-MILES: Photometric predictions based on E-MILES SEDs*).

The set includes different widely used prescriptions for the stellar IMF, following the functional forms introduced in the classic works of Vazdekis (1996), Kroupa (2001) and Chabrier (2003) (Fig. 4.6), in particular:

- **Unimodal IMF**. Single power law in which the logarithmic slope acts as the sole free parameter. The standard Salpeter IMF corresponds to the specific case in which the slope is set to 1.3.
- **Bimodal IMF**. Same power-law behaviour as the unimodal form at stellar masses above $0.6\,M_{\odot}$, but flatter slope at lower masses, decreasing the contribution.

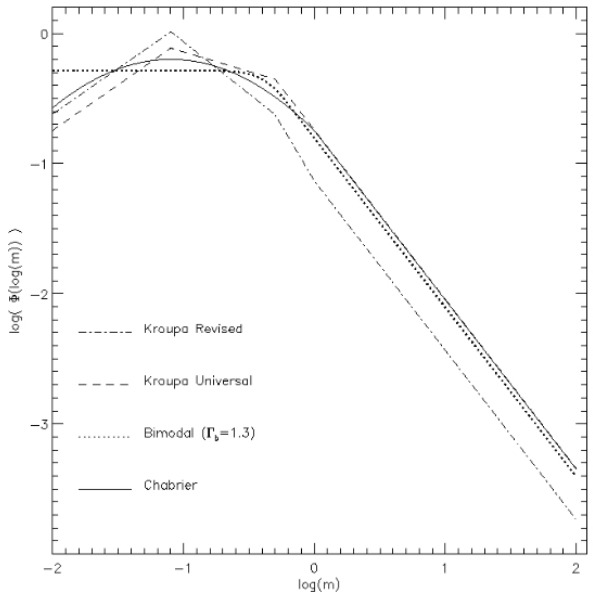

Figure 4.6: Comparison of the IMF functional forms adopted in the MILES models. Taken from *E-MILES: Photometric predictions based on E-MILES SEDs*

- **Kroupa (2001) Universal IMF**. Multiple-power-law IMF that resembles the Salpeter form for masses exceeding $0.5\,M_{\odot}$, but incorporates two segments with shallower slope in the low-mass regime.
- **Kroupa (2001) Revised IMF**. Also described by a multi-part power law, this version includes corrections that account for the expected impact of unresolved binary systems on the inferred single-star IMF.
- **Chabrier (2003) IMF**. A log-normal distribution at sub-solar stellar masses, joined smoothly to a power-law tail at higher masses.

The aim was to determine the values of $\Upsilon_{*,b}$ and $\Upsilon_{*,d}$ in the R-band, corresponding to the ages and metallicities reported in the stellar-population studies of NGC 1366 by M08; M15. For the bulge, the central measurements from M08 were adopted (Tab. 2.5), while for the disc the estimates at r_{d95}, the radius where the disc contributes more than 95% of the galaxy's surface brightness, from M15 were used (Tab. 2.6), as they provide the most reliable constraints for the disc population.

Since the E-MILES predictions are tabulated on a discrete age–metallicity grid, an interpolation routine was developed to compute the required mass-to-light ratios. For each component, a set of neighbouring grid points is selected so as to bracket the target age and metallicity values. In the case of the bulge, the points (5.0, 0.40), (5.5, 0.40), and (5.0, 0.26) are used, whereas for the disc the selected points are (7.5, −0.25), (8.0, −0.25), and (7.5, −0.35). As an example, Tab. 4.2 lists the mass-to-light ratios

(Age_b,$[Z/\mathrm{H}]_b$) target	Age_b [Gyr]	$[Z/\mathrm{H}]_b$ [dex]	$\Upsilon_{*,b}$	(Age_b,$[Z/\mathrm{H}]_b$) target	Age_d [Gyr]	$[Z/\mathrm{H}]_d$ [dex]	$\Upsilon_{*,d}$
(5.10, 0.39)	5.00	0.26	2.95	(7.60, -0.26)	7.50	−0.35	2.66
(5.10, 0.39)	5.00	0.40	3.22	(7.60, -0.26)	7.50	−0.25	2.84
(5.10, 0.39)	5.50	0.40	3.35	(7.60, -0.26)	8.00	−0.25	2.96

Table 4.2: Mass-to-light ratios in the R-band for the three neighbouring grid points used in the interpolation of the bulge and disc values, for the Kroupa Revised IMF (BaSTI isochrones).

IMF	Age_b [Gyr]	$[Z/\mathrm{H}]_b$ [dex]	$\Upsilon_{*,b}$	Age_d [Gyr]	$[Z/\mathrm{H}]_d$ [dex]	$\Upsilon_{*,d}$
Unimodal	5.10	0.39	3.43 ± 0.18	7.60	−0.26	3.06 ± 0.13
Bimodal	5.10	0.39	2.34 ± 0.12	7.60	−0.26	2.08 ± 0.09
Kroupa Universal	5.10	0.39	2.33 ± 0.12	7.60	−0.26	2.07 ± 0.09
Kroupa Revised	5.10	0.39	3.23 ± 0.17	7.60	−0.26	2.84 ± 0.12
Chabrier	5.10	0.39	2.13 ± 0.11	7.60	−0.26	1.91 ± 0.08

Table 4.3: Stellar mass-to-light ratios Υ_{*i} estimated through interpolation for the bulge and disc components, derived from the MILES photometric predictions using the ages and metallicities adopted from M08; M15.

at the aforementioned neighbouring grid points for the bulge component, in the case of the Kroupa Revised IMF.

The routine reads the relevant MILES table for a given IMF, extracts the corresponding Υ_{*i} values in the R-band for the chosen neighbouring grid points, and performs a two-dimensional linear interpolation. The uncertainty associated with each interpolated mass-to-light ratio is estimated from the standard deviation of the selected neighbouring points. This procedure was applied for all available IMFs (under the BaSTI isochrone sets), and the resulting interpolated values were later used in the dynamical modelling of NGC 1366.

The estimates of the mass-to-light ratios Υ_{*i} are reported in Tab. 4.3. The revised Kroupa IMF is adopted as the starting point for parameter exploration because it provides the highest Υ_{*i} among the analysed IMFs, with the sole exception of the Salpeter-like Unimodal IMF. A preliminary inspection with $k_i = \pm 1.0$ (Fig. 4.7) shows that the models require relatively high stellar masses, and therefore high Υ_{*i} for fixed

L_{*i}, in order to approach the observed amplitude of the velocity dispersion profile $\sigma_{\rm los}$ (panels on the right).

In order to increase the mass-to-light ratios Υ_{*i} in a physically meaningful way, the mass fractions of the two components are kept fixed to the values derived from the mass-to-light ratios obtained under the assumption of a revised Kroupa IMF. For all the IMF estimates considered, however, these fractions remain consistent at $R_b = 0.4$ and $R_d = 0.6$. Following this approach, the mass-to-light ratios that provide the best match to the observational data (i.e. the line-of-sight velocity dispersion $\sigma_{\rm los}$ profile) are $\Upsilon_{*,b} = 4.4$ and $\Upsilon_{*,d} = 4.0$, as shown in Fig. 4.10.

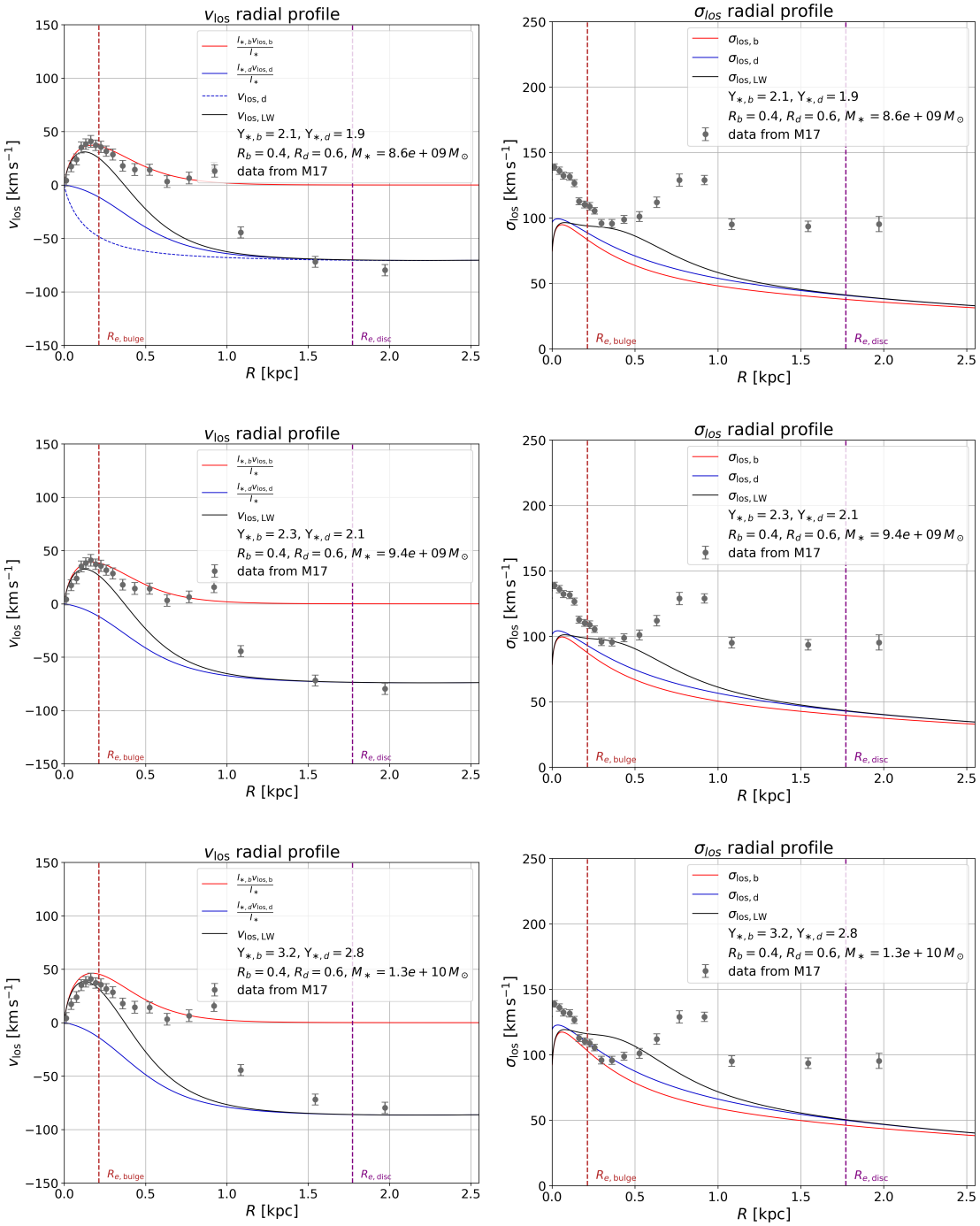

Figure 4.7: Stellar line-of-sight velocity profile $v_{\rm los}$ (*left column*) and velocity dispersion profile $\sigma_{\rm los}$ (*right column*) along the major axis, for two-component models with $R_b = 0.4, R_d = 0.6$ and $k_i = \pm 1.0$. Three different configurations are shown: *top*: $\Upsilon_{*,b} = 2.1, \Upsilon_{*,d} = 1.9$ (Chabrier); *middle*: $\Upsilon_{*,b} = 2.3, \Upsilon_{*,d} = 2.1$ (Kroupa); *bottom*: $\Upsilon_{*,b} = 3.2, \Upsilon_{*,d} = 2.8$ (Kroupa rev.). In the top-left panel, for comparison, both the $v_{{\rm los},d}$ and $\frac{I_{*,d}}{I_*}\,v_{{\rm los},d}$ profiles are shown. In all other panels, only the luminosity-weighted quantities are plotted, since in this form the total observed profile is directly given as sum of the bulge and disc contributions.

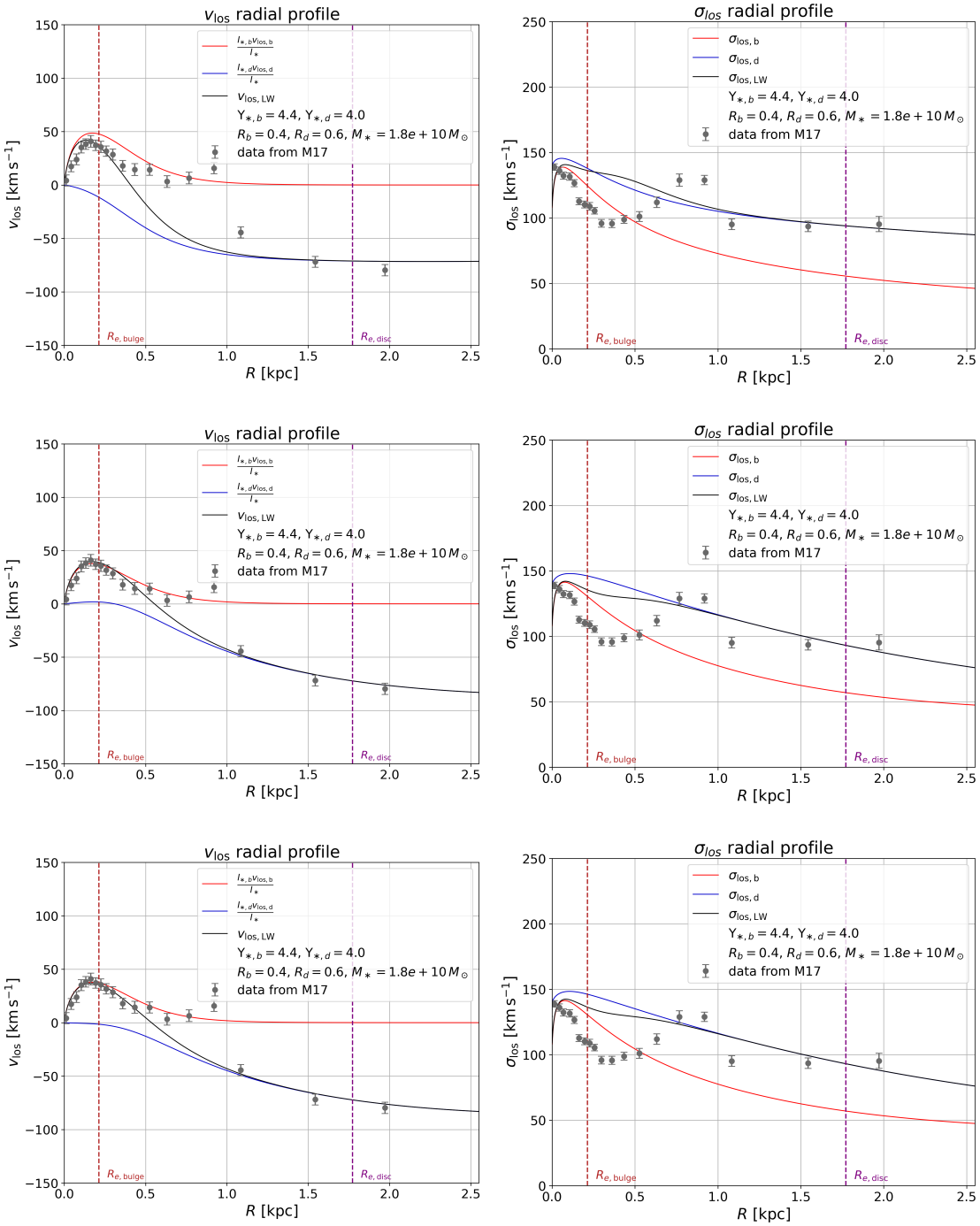

Figure 4.8: Stellar line-of-sight velocity profile $v_{\rm los}$ (*left column*) and velocity dispersion profile $\sigma_{\rm los}$ (*right column*) along the major axis, for two-component models with $\Upsilon_{*,b} = 4.4, \Upsilon_{*,d} = 4.0$. Three different choices of the functional form of the disc Satoh parameter k_d are shown: *top*: $k_b = 0.9$, $k_d = -0.7$; *middle*: $k_b = 0.7$, $k_d = 0.9 \times k_{d1}$; *bottom*: $k_b = 0.7$, $k_d = 0.9 \times k_{d2}$.

4.2.3 Kinematical decomposition for the case study

All the previous investigations were performed assuming a constant Satoh parameter over the whole space, such that

$$\delta_i(R, z) = 1, \qquad k_i = \lambda_i. \tag{4.13}$$

While the choice of $k_b = \text{const}$ is reasonable, as the bulge primarily dominates the central regions and its contribution rapidly decreases at larger radii, early attempts showed that a constant k_d could not reproduce the observed line-of-sight velocity $v_{\rm los}$ values at intermediate radii ($R \sim 0.5$–0.8 kpc). In this region, the bulge contribution is slightly positive, therefore the disc must provide a counteracting or near-zero contribution; at larger radii ($R \gtrsim 1$ kpc) $v_{\rm los}$ is largely negative, the disc dominates, and it should be fully counter-rotating with $k_d \sim -1$, satisfactorily accounting for the observed $v_{\rm los}$.

To address this, variable k_i profiles were tested following the prescriptions described in Subsec. 3.5.2. Several functional forms for $k_d(R)$ were explored, chosen to achieve the desired radial behaviour of $v_{\rm los}$. In particular, the aim was to shift outwards the radius at which the model $v_{\rm los}$ approximately vanishes and better reproduce the observed kinematics.

$$k_{\rm d1}(R) = -1 + \exp\big[-(R - 0.5)\big], \tag{4.14}$$
$$k_{\rm d2}(R) = -1 + \exp\big[-(R - 0.5)\big] - \exp\big[-R/r_*\big], \tag{4.15}$$
$$k_{\rm d3}(R) = -1 + \exp\big[-(R - 0.75)\big] - 2\exp\big[-R/r_*\big]. \tag{4.16}$$

The motivation behind these forms, presented in Fig. 4.9, is as follows:

- The first term in all functions would ensure that $k_d \to -1$ at large radii, reproducing the fully counter-rotating behaviour of the disc where it dominates the kinematics;
- The exponential terms subtracted in $k_{\rm d2}$ and $k_{\rm d3}$ aim to remove the small positive contribution of the disc in the central regions;
- The shift in the exponent (e.g., 0.5 or 0.75 kpc) is tuning the zero-crossing point of $v_{\rm los}$.

After testing all the different functional forms for $k_d(R)$ (Fig. 4.8), $k_{\rm d3}$ is found to provide an improvement, as shown in Fig. 4.10. This implementation ensures a smooth radial variation of k_d, producing a $v_{{\rm los},d}$ highly counter-rotating at large radii and reducing its contribution in the inner regions, in line with the observational constraints on $v_{\rm los}$ discussed before.

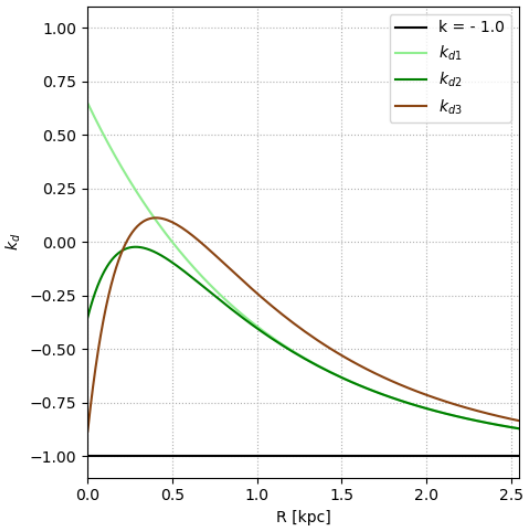

Figure 4.9: Radial profiles of the disc Satoh parameter $k_d(R)$. The constant profile $k = -1.0$ (black) is compared with the variable forms tested: $k_{\mathrm{d1}}(R)$ (light green), $k_{\mathrm{d2}}(R)$ (green), and $k_{\mathrm{d3}}(R)$ (brown).

4.3 Results

The results of the modelling for the galaxy NGC 1366 are presented here by comparing them with the kinematic measurements along the major axis of NGC 1366. The model is tested against the line-of-sight velocity (v_{los}) data along the negative semi-major axis and against the velocity dispersion (σ_{los}) data along the entire major axis. For simplicity of visualisation in the plots, however, both profiles are displayed using only the negative semi-axis, mirrored to positive R values.

The present study tests whether a two-component model, constrained by the photometric decomposition and governed by a minimal set of free parameters, is able to reproduce the observed velocity v_{los} and velocity dispersion σ_{los} profiles.

The best result, obtained with the set of parameters listed in Tab. 4.4 as discussed in Subsec. 4.2.2 and Subsec. 4.2.3, is shown in Fig. 4.10 and Fig. 4.11.

4.3.1 Discussion and conclusions

Within the explored family of two-component models, the configuration that yields the closest agreement with the observations adopts the mass-to-light ratios $\Upsilon_{*,b} = 4.4$ and $\Upsilon_{*,d} = 4.0$, together with the Satoh parameters $k_b = 0.7$ and $k_d(R) = 0.9\, k_{d3}$, where k_{d3} is a function of the radial coordinate. These values correspond to the parameter combination that provides the closest overall reproduction of the kinematic fields of NGC 1366.

Post-Processing (weights)	$L_{*b} = 1.46\ L_\odot$	$L_{*d} = 2.90\ L_\odot$
	$\Upsilon_{*b} = 4.4$	$\Upsilon_{*d} = 4.0$
	$R_b = 0.4$	$R_d = 0.6$
	$k_b = 0.7$	$k_d = 0.9 k_{d3}$
Post-Processing (physical scales)	$M_* = 1.80 \times 10^{10}\,\mathrm{M}_\odot$	
	$r_* = R_{e,b} = 0.213$ kpc	

Table 4.4: Weights, kinematical and physical parameters in the Post Processing module that characterise the two-component model that best describes the data: stellar luminosities L_{*i}, mass-to-light ratios Υ_{*i}, mass fractions R_i, Satoh parameters k_i, total stellar mass M_* and stellar scale length r_*.

This model succeeds in reproducing the observed line-of-sight velocity profile $v_{\rm los}$ with reasonable accuracy. The overall shape of the rotation curve, including the steep rise in the central region, is matched well, with the exception of two datapoints in the interval 0.75 kpc $\lesssim R \lesssim$ 1.00 kpc. In the innermost radii, where the dynamical structure is dominated by the bulge, the assumption of a constant Satoh parameter k_b proves adequate, indicating that the model is able to reconstruct the kinematics of the bulge component. At large radii, beyond $R \gtrsim 1\,$kpc, the model also follows the observed decline of the rotation curve, further supporting its ability to reproduce the global behaviour of the velocity field.

The velocity dispersion profile $\sigma_{\rm los}$, however, is not successfully reproduced by any of the two-component configurations explored in this work. Although the adopted mass-to-light ratios allow the model to recover both the height of the central peak and the amplitude of the dispersion at large radii (near $R \approx 1R_{e,d}$), the predicted profile remains too smooth compared to the observed one. Most notably, the characteristic off-centre peaks in $\sigma_{\rm los}$, i.e. the defining kinematic signature of 2σ systems, are entirely absent. Instead of the sharp decrease followed by a secondary rise seen in the data, the model predicts a shallow plateau extending to $R \approx 0.6$ kpc, produced by the counter rotation between bulge and disc. The observed peaks, however, lie at significantly larger radii, beyond $3R_{e,b}$, where the bulge contribution to $v_{\rm los}$ is nearly zero. At those radii, the bulge cannot contribute to the formation of a second peak in $\sigma_{\rm los}$, which requires the overlap of two components with comparable light and opposite rotational velocities.

Additional support for this interpretation comes from photometry. In the same radial range where the off-centre peak is detected (0.75 kpc $\lesssim R \lesssim$ 1.00 kpc), the bulge–disc decomposition of the surface brightness profile exhibits significant residuals

(in Fig. 2.2). This mismatch indicates that the assumed two-component photometric structure is itself insufficient, and it mirrors the insuccess revealed by the dynamical modelling.

Taken together, these results show that a simple bulge–disc configuration is not capable of reproducing the kinematic complexity observed in NGC 1366. In particular, the inability to generate off-centre dispersion peaks, a characteristic feature of 2σ galaxies in which two stellar discs counter-rotate and overlap in projection, strongly suggests that NGC 1366 hosts a more intricate multi-component structure, likely involving more than a single disc component.

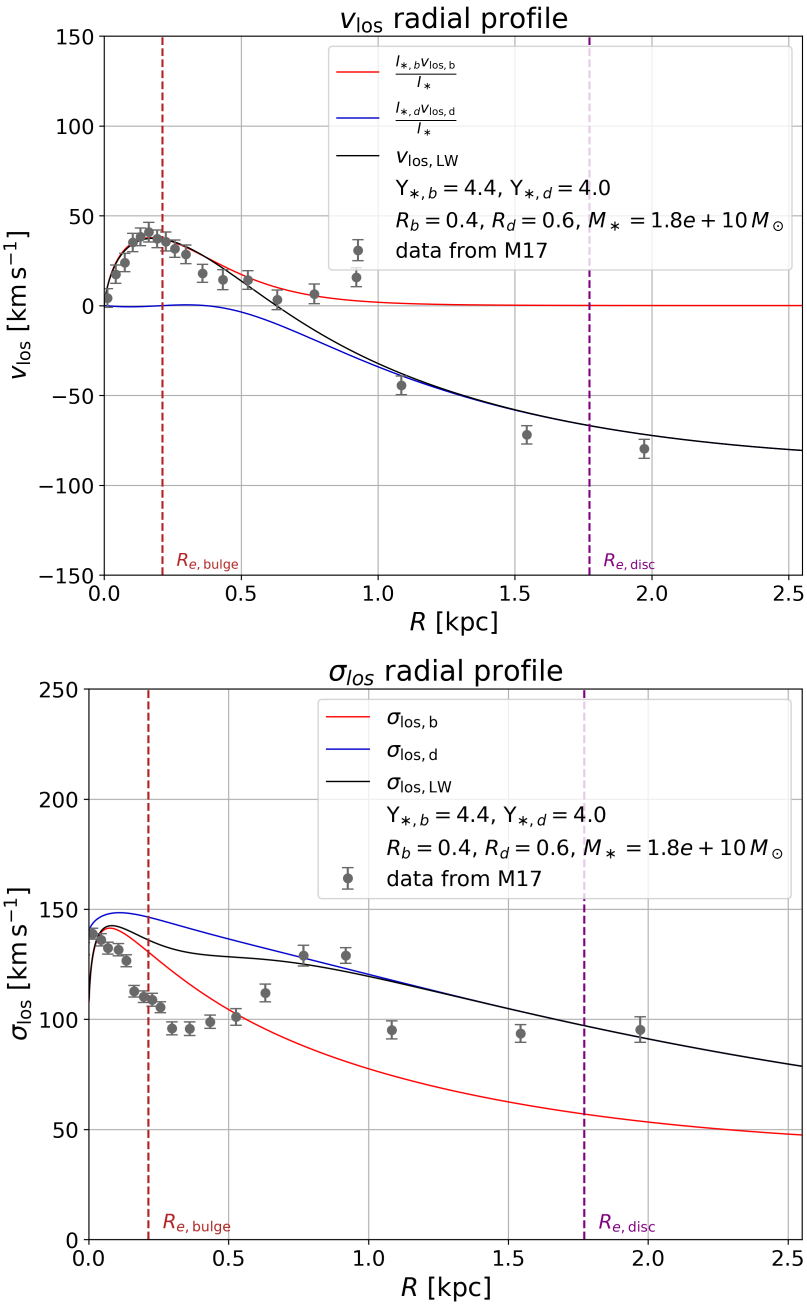

Figure 4.10: Radial profiles along the major axis, with $\Upsilon_{*,b} = 4.4, \Upsilon_{*,d} = 4.0$, $k_b = 0.7, k_d = 0.9k_{d3}$. *Top panel*: stellar line-of-sight velocity profile $v_{\rm los}$. *Bottom panel*: stellar line-of-sight velocity dispersion profile $\sigma_{\rm los}$. Gray points indicate observational data taken from M17.

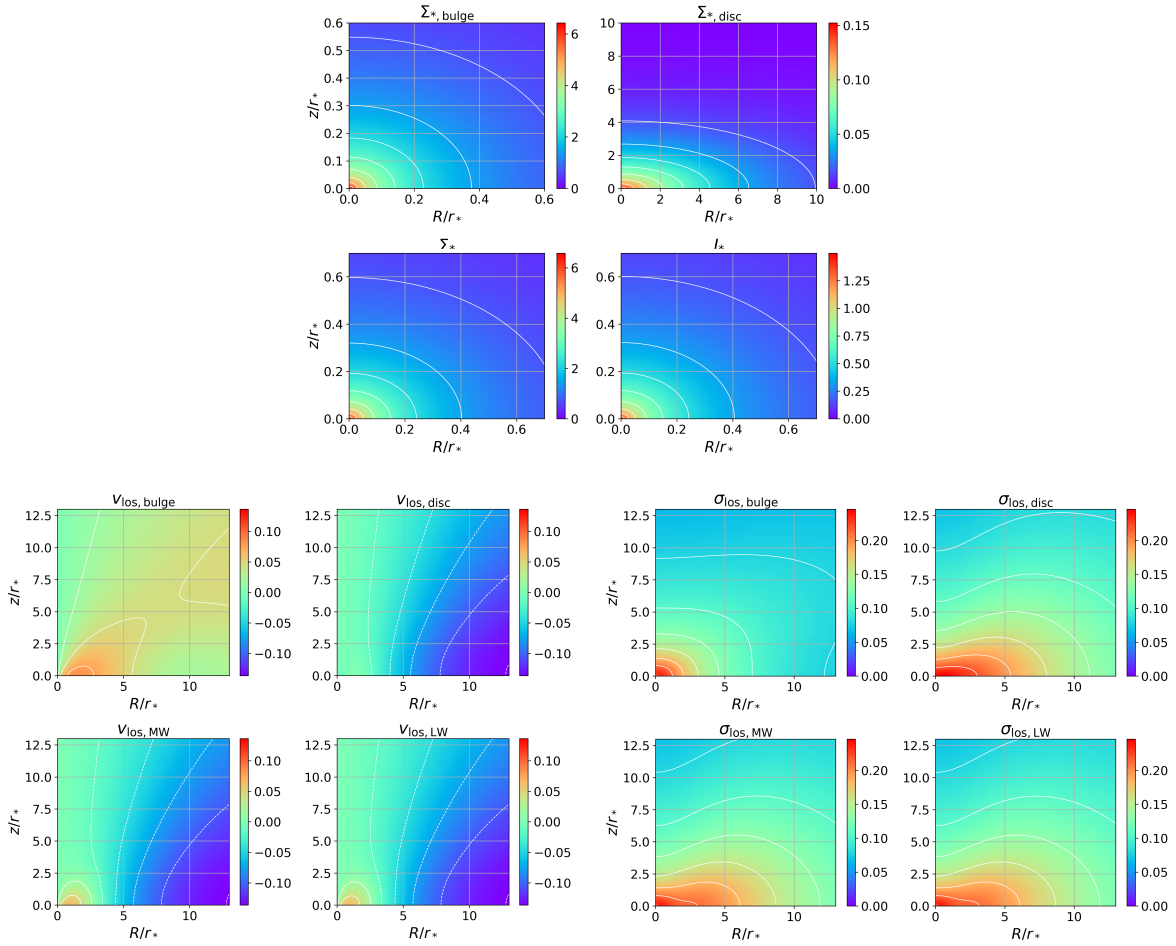

Figure 4.11: Two–dimensional maps in the $(\tilde{R}, \tilde{z})$ plane of scaled and adimensional projected quantities computed for the best fit model (parameters in Tab. 4.4): surface density distribution, rotational velocity and velocity dispersion, for each component and for mass-weighted and luminosity-weighted total.

Summary and conclusions

The purpose of this Master's thesis is to employ the methodology of dynamical modelling, specifically through the numerical code `JASMINE2` (Jeans AxiSymmetric Models of galaxies IN Equilibrium), to probe the internal structure and intricate dynamics of the lenticular galaxy NGC 1366. This galaxy, located in the Fornax cluster, belongs to the class of multi-spin early-type galaxies, known to host counter-rotating (CR) components. Previous spectroscopic studies found signatures of counter rotation in NGC 1366: the disc component, the more luminous structure, is rotating in the opposite direction relative to the bulge. Furthermore, a subsequent spectroscopic analysis of the spectrum at two positions centred at $R \approx 1$ kpc and $R \approx 2$ kpc revealed the presence of two CR stellar components in the disc region, indicating an even more complex configuration.

This work investigates whether the observed kinematic features can be reproduced by the simplest two-component axisymmetric model composed only of a bulge and a disc. By comparing the model predictions with the measured profiles for the line-of-sight velocity $v_{\rm los}$ and the line-of-sight velocity dispersion $\sigma_{\rm los}$, it is possible to evaluate the viability of this simplified configuration as a dynamical representation of the galaxy and to constrain key physical parameters, such as the stellar mass-to-light ratios Υ_{*i}, the mass fractions R_i, and the total stellar mass of the system M_*.

This study made use of the output from a single `JASMINE2` run, which produced the progenitor model of a family of two-component systems, all sharing the same structural parameters for the scaled stellar densities $\tilde{\varrho}_{*i}$.

Information derived from the available observational data, such as the photometric bulge–disc decomposition and the luminosities of the components, was introduced as fixed input to the model in order to produce comparable observables.

Then, within the Post-Processing module, additional routines were developed to generate a set of distinct models for the galaxy, varying two free parameters: the mass-to-light ratios Υ_{*i}, accounting for the stellar population properties, and the Satoh parameters k_i, for the decomposition of the azimuthal motion. In order to construct the final projected kinematic fields, the routines handled the implementation of the weighting scheme and the conversion from dimensionless scaled quantities to physical units (also through the resulting value for the stellar mass M_* and the chosen scale length r_*).

An interpolation routine was also implemented to have an initial estimate for one of the free parameters, the R-band stellar mass-to-light ratios Υ_{*i}. The values are obtained by interpolating across the discrete age–metallicity grid provided by the E-MILES photometric predictions.

Within the set of two-component models, the configuration yielding the closest match adopts the mass-to-light ratios $\Upsilon_{*,b} = 4.4$ and $\Upsilon_{*,d} = 4.0$, with Satoh parameters $k_b = 0.7$ and $k_d(R) = 0.9 \times k_{d3}$, where k_{d3} is a function of the radial coordinate.

This model reproduces the observed line-of-sight velocity profile $v_{\rm los}$ with reasonable success, missing only two datapoints between 0.75 kpc $\lesssim R \lesssim$ 1.00 kpc. In the inner regions, where the dynamics of the system is proved to be dominated by the bulge contribution, the observed velocity profile is well reproduced by assuming a constant k_b, suggesting that the model is able to successfully reconstruct the kinematics of the bulge.

However, none of the explored configurations is able to reproduce the observed velocity dispersion profile $\sigma_{\rm los}$. The mass-to-light ratios Υ_{*i} chosen for the best-result model allow to recover both the height of the central peak and the amplitude of the velocity dispersion at large radii (near $R = 1R_{e,d}$), but the overall smooth behaviour of the predicted profile does not match the data. Crucially, the two-component model fails to replicate the distinctive off-centre kinematic peaks observed in the $\sigma_{\rm los}$ radial profile. The modelled velocity dispersion profile $\sigma_{\rm los}$, at radii immediately beyond the central maximum, instead of a sharp decrease, presents a shallow plateau out to $R = 0.6$ kpc, produced by the counter rotation between bulge and disc. The observed off-centre peaks occur, instead, at larger radii, beyond $3R_{e,b}$, where the bulge contribution to the projected velocity $v_{\rm los}$ is almost zero, and therefore it cannot generate the second peak in the velocity dispersion $\sigma_{\rm los}$, which arises where two components with comparable light have rotational velocity with similar amplitude but opposite sign.

Moreover, in the same radial range where the off-centre peak is detected, the photometric decomposition also fails to successfully reproduce the surface brightness profile of the galaxy. At 0.75 kpc $\lesssim R \lesssim$ 1.00 kpc, the bulge–disc decomposition shows non negligible residuals (i.e. difference between model and data radial profiles). This points out that the inability of the two-component model to reproduce the kinematic fields, highlighted in the present study, is consistent with the indications emerging from the photometric analysis.

Consequently, the failure of the two-component model to capture the off-centre kinematic peaks, a defining signature of 2σ galaxies (i.e. systems hosting two CR stellar discs overlapping in projection), strongly suggests that the actual structure of NGC 1366 is more complex than a simple bulge-disc configuration.

The modelling procedure also reveals a necessary dynamical constraint: a lower limit on the bulge mass fraction R_b is required for the Satoh prescription for the decomposition of azimuthal motion to be applicable. Under the adopted Satoh k-

decomposition, and independently of any other parameter choices made in the Post-Processing stage, the condition $R_b > 0.336$ must be satisfied.

Furthermore, it is worth noting that the best-result model required significantly high stellar mass-to-light ratios ($\Upsilon_{*,b} = 4.4$, $\Upsilon_{*,d} = 4.0$), exceeding the predictions derived from the E-MILES stellar populations models.

The conclusions drawn are subject to the limitations imposed by the chosen modelling framework.

Firstly, the gravitational potential used was intentionally simplified, comprising only the two stellar components (bulge and disc), while neglecting the potential contributions of a surrounding Dark Matter (DM) halo and a central supermassive Black Hole (BH). Their exclusion simplifies the computation, but may introduce inaccuracies in the predicted kinematic profiles, both at small radii, where the BH is expected to dominate, and in the outskirts, where the DM halo contribution becomes important.

The required high stellar mass-to-light ratios Υ_{*i} represent an indication that the two-component stellar model is attempting to compensate for missing complexity or missing dynamical mass. The high values might be compensating for the gravitational influence of the omitted DM halo, or they could be artificially higher because the model is missing the natural increase in velocity dispersion provided by the superposition along the line of sight of velocities from a third CR stellar component. Finally, the modelling operated under the assumption of a two-integral distribution function $f(E, J_z)$; allowing the radial velocity dispersion (σ_R) to differ from the vertical component (σ_z) could instead help increase the line-of-sight velocity dispersion $\sigma_{\rm los}$ in the central region, potentially reducing the high stellar mass-to-light ratios Υ_{*i} required by the current models. Furthermore, it is important to stress that, within the parameter exploration, a degeneracy was observed in the effect on the rotation velocity $\bar{v}_\phi$ between the mass-to-light ratios Υ_{*i} and the Satoh parameters k_i. This degeneracy complicates the unique identification of the physical parameters that best describe the system and their interpretation.

The outcome of this thesis suggests that future dynamical studies of NGC 1366 must incorporate increased complexity to fully resolve its kinematics.

The most critical recommendation is to move beyond the simplified two-component model and implement a three-component stellar model within the `JASMINE2` framework. This model should explicitly incorporate the younger, kinematically-decoupled counter-rotating stellar component identified through spectroscopic studies.

Furthermore, to refine the constraints on the mass-to-light ratios and accurately model the galaxy's gravitational support, subsequent iterations of the model must include the gravitational influence of a DM halo and of the central BH. These inclusions are essential to assess whether the high stellar mass-to-light ratios (Υ_{*i}) required in the current stellar-only model are truly physical or merely compensating for missing dynamical mass.

Finally, considering the inability of the two-integral, axisymmetric approach to cap-

ture the off-centre kinematic peaks, future research should explore more sophisticated dynamical techniques. This may involve employing three-integral distribution functions or running dedicated N-body simulations of gas accretion and counter-rotating disc formation.

The current two-component model serves as a necessary blueprint, setting some constraints and providing useful suggestions. However, its limited complexity proves insufficient to reproduce the detailed kinematical features observed in the galaxy. The comparison between data and best-result model reveals dynamical signatures that seem to require an additional, counter-rotating component; without it, the model inevitably smooths over the complexity encoded in the observed kinematics, which retain a far more intricate record of the galaxy's evolutionary past. This outcome points toward the need for more sophisticated multi-component dynamical modelling to capture the full complexity of NGC 1366.

Bibliography

Algorry, Diego G., Julio F. Navarro, Mario G. Abadi, Laura V. Sales, Matthias Steinmetz, and Florian Piontek (2014). "Counterrotating stars in simulated galaxy discs". In: *Monthly Notices of the Royal Astronomical Society* 437.4, pp. 3596–3602. DOI: 10.1093/mnras/stt2154.

Bertola, F., P. Cinzano, E. M. Corsini, A. Pizzella, M. Persic, and P. Salucci (1996). "Counter-rotating Stellar Disks in Early-Type Spirals: NGC 3593". In: *The Astrophysical Journal* 458, pp. L67–L70. DOI: 10.1086/309924.

Bettoni, D., G. Galletta, and S. García-Burillo (2003). "Counter-rotation in disc galaxies: gas accretion from companions". In: *Astronomy and Astrophysics* 405, pp. 5–16. DOI: 10.1051/0004-6361:20030559.

Bettoni, D., G. Galletta, and F. Prada (2001). "The visible environment of galaxies with counterrotation". In: *Astronomy & Astrophysics* 374, pp. 83–92. DOI: 10.1051/0004-6361:20010691.

Binggeli, Bruno and L. Margaret Cameron (1991). "Structure and stellar content of dwarf elliptical galaxies. I - UBV photometry of 16 Virgo cluster dwarfs". In: *Astronomy and Astrophysics* 252, pp. 27–44.

Binney, James (1978). "The dynamics of elliptical galaxies". In: *Monthly Notices of the Royal Astronomical Society* 183, pp. 501–514. DOI: 10.1093/mnras/183.3.501.

— (2005). "The physics of early-type galaxies". In: *Monthly Notices of the Royal Astronomical Society* 363, pp. 937–942. DOI: 10.1111/j.1365-2966.2005.09522.x.

Binney, James and Michael Merrifield (1998). *Galactic Astronomy*. Princeton Series in Astrophysics. Princeton, NJ: Princeton University Press, pp. xiii + 796. ISBN: 0-691-02565-7.

Binney, James and Scott Tremaine (2008). *Galactic Dynamics*. 2nd. Princeton, NJ: Princeton University Press.

Bois, Maxime, Eric Emsellem, Frédéric Bournaud, Katherine Alatalo, Leo Blitz, Martin Bureau, Michele Cappellari, Roger L. Davies, Timothy A. Davis, P. Tim de Zeeuw, Pierre-Alain Duc, Sadegh Khochfar, Davor Krajnović, Harald Kuntschner, Pierre-Yves Lablanche, Richard M. McDermid, Raffaella Morganti, Thorsten Naab, Tom Oosterloo, Marc Sarzi, Nicholas Scott, Paolo Serra, Anne-Marie Weijmans, and Lisa M. Young (2011). "The ATLAS^{3D} project – VI. Simulations of binary galaxy mergers and the link with fast rotators, slow rotators, and kinematically decoupled cores". In: *Monthly Notices of the Royal Astronomical Society* 416, pp. 1654–1679. DOI: 10.1111/j.1365-2966.2011.19113.x.

Brown, R. V. E., R. A. M. Walterbos, and R. C. Jr. Kennicutt (1992). "Counter-rotating gaseous disks in the "Evil Eye" galaxy NGC 4826". In: *Nature* 360, pp. 442–445. DOI: 10.1038/360442a0.

Bundy, K., M. A. Bershady, D. R. Law, and et al. (2015). "Overview of the MaNGA Survey: Mapping Nearby Galaxies at Apache Point Observatory". In: *The Astrophysical Journal* 798.1, p. 7. DOI: 10.1088/0004-637X/798/1/7.

Caon, N., M. Capaccioli, and M. D'Onofrio (1993). "On the shape of the light profiles of early type galaxies". In: *Monthly Notices of the Royal Astronomical Society* 265.4, pp. 1013–1021.

Capaccioli, Massimo (1987). "Surface Photometry of Elliptical Galaxies". In: *Structure and Dynamics of Elliptical Galaxies*. Ed. by T. de Zeeuw. Vol. 127. IAU Symposium. Dordrecht: Reidel, pp. 47–60.

— (1989). "Structure of Elliptical Galaxies". In: *The World of Galaxies (Le Monde des Galaxies)*. Ed. by Harold G. Corwin and Luc Bottinelli. New York: Springer, pp. 208–227.

Cappellari, Michele (2008). "Measuring the inclination of early-type galaxies via anisotropic Jeans models of stellar kinematics". In: *Monthly Notices of the Royal Astronomical Society* 390.1, pp. 71–86. DOI: 10.1111/j.1365-2966.2008.13752.x.

— (2016). "Structure and Kinematics of Early-Type Galaxies from Integral-Field Spectroscopy". In: *Annual Review of Astronomy and Astrophysics* 54, pp. 597–665. DOI: 10.1146/annurev-astro-082214-122432.

Cappellari, Michele, Eric Emsellem, Roland Bacon, Martin Bureau, Roger L. Davies, P. Tim de Zeeuw, Jesús Falcón-Barroso, Davor Krajnović, Harald Kuntschner, Richard M. McDermid, Reynier F. Peletier, Marc Sarzi, Remco C. E. van den Bosch, and Glenn van de Ven (2007). "The SAURON project - X. The orbital anisotropy of elliptical and lenticular galaxies: revisiting the (V/σ, ε) diagram with integral-field stellar kinematics". In: *Monthly Notices of the Royal Astronomical Society* 379.2, pp. 418–444. DOI: 10.1111/j.1365-2966.2007.11963.x.

Cappellari, Michele, Eric Emsellem, Davor Krajnović, Richard M. McDermid, Nicholas Scott, Gijs A. Verdoes Kleijn, Lisa M. Young, Katherine Alatalo, Leo Blitz, Maxime Bois, Frédéric Bournaud, Martin Bureau, Roger L. Davies, Timothy A. Davis, P. T. de Zeeuw, Pierre-Alain Duc, Sadegh Khochfar, Harald Kuntschner, Raffaella Morganti, Thorsten Naab, Tom Oosterloo, Marc Sarzi, Paolo Serra, Anne-Marie Weijmans, and P. T. de Zeeuw (2011). "The ATLAS^{3D} project – I. A volume-limited sample of 260 nearby early-type galaxies: science goals and selection criteria". In: *Monthly Notices of the Royal Astronomical Society* 413.2, pp. 813–836. DOI: 10.1111/j.1365-2966.2010.18174.x.

Cappellari, Michele, Nicholas Scott, Katherine Alatalo, Leo Blitz, Maxime Bois, Frédéric Bournaud, Martin Bureau, Alison F. Crocker, Roger L. Davies, Timothy A. Davis, P. Tim de Zeeuw, Eric Emsellem, Sadegh Khochfar, Davor Krajnović, Harald Kuntschner, Richard M. McDermid, Raffaella Morganti, Thorsten Naab, Tom Oosterloo, Marc Sarzi, Paolo Serra, Anne-Marie Weijmans, and Lisa M. Young (2013). "The ATLAS^{3D} project – XV. Benchmark for early-type galaxies dynamics and scaling relations from Jeans and Schwarzschild modelling". In: *Monthly Notices of the Royal Astronomical Society* 432, pp. 1709–1741. DOI: 10.1093/mnras/sts384.

Caravita, Caterina (2022). "An efficient Jeans modelling of axisymmetric galaxies with multiple stellar components". PhD thesis. Alma Mater Studiorum — Università di Bologna. DOI: 10.48676/unibo/amsdottorato/10433.

Caravita, Caterina, Luca Ciotti, and Silvia Pellegrini (2021). "Jeans modelling of axisymmetric galaxies with multiple stellar populations". In: *Monthly Notices of the Royal Astronomical Society* 506.1, pp. 1480–1497. DOI: 10.1093/mnras/stab1786.

Chabrier, Gilles (2003). "The Galactic Disk Mass Function: Reconciliation of the Hubble Space Telescope and Nearby Determinations". In: *Publications of the Astronomical Society of the Pacific* 115, pp. 763–795. DOI: 10.1086/376392.

Ciotti, Luca (1991). "Stellar systems following the $R^{1/m}$ luminosity law". In: *Astronomy & Astrophysics* 249, pp. 99–106.

Ciotti, Luca, Antonio Mancino, Silvia Pellegrini, and Azadeh Ziaee Lorzad (2021). "Two-component galaxy models with a central BH – II. The ellipsoidal case". In: *Monthly Notices of the Royal Astronomical Society* 500.1, pp. 1054–1070. DOI: 10.1093/mnras/staa3338.

Ciotti, Luca, Antonio Mancino, Silvia Pellegrini, Azadeh Ziaee Lorzad, and Caterina Caravita (2022). "A parameter space exploration of high-resolution numerically evolved early-type galaxies including AGN feedback and accurate dynamical treatment of stellar orbits". In: *Monthly Notices of the Royal Astronomical Society* 512.4, pp. 5102–5122. DOI: 10.1093/mnras/stac833.

Ciotti, Luca and Silvia Pellegrini (1996). "The energetics of flat and rotating early-type galaxies and their X-ray luminosity". In: *Monthly Notices of the Royal Astronomical Society* 279.1, pp. 240–248. DOI: 10.1093/mnras/279.1.240. URL: https://academic.oup.com/mnras/article/279/1/240/1358281.

Ciri, R., D. Bettoni, and G. Galletta (1995). "A Massive Counter-Rotating Gas Disk in a Spiral Galaxy". In: *Nature* 375, pp. 661–663. DOI: 10.1038/375661a0.

Coccato, L., L. Morelli, E. M. Corsini, and et al. (2011). "Kinematic and stellar population properties of the counter-rotating components in the S0 galaxy NGC 5719". In: *Monthly Notices of the Royal Astronomical Society* 412, pp. L113–L117. DOI: 10.1111/j.1745-3933.2011.01016.x.

Corsini, E. M. (2014). "Counter-Rotation in Disk Galaxies". In: *Multi-Spin Galaxies*. Ed. by Enrichetta Iodice and Enrico Maria Corsini. Vol. 486. ASP Conference Series. Proceedings of the conference *Multi-Spin Galaxies*. San Francisco: Astronomical Society of the Pacific, pp. 51–64. URL: https://ui.adsabs.harvard.edu/abs/2014ASPC..486...51C/abstract.

Corsini, E. M., V. P. Debattista, and J. A. L. Aguerri (2003). "Direct Confirmation of Two Pattern Speeds in the Double-barred Galaxy NGC 2950". In: *The Astrophysical Journal* 599, pp. L29–L32. DOI: 10.1086/381080. URL: https://ui.adsabs.harvard.edu/abs/2003ApJ...599L..29C/abstract.

Crocker, Alison F., Hyunjin Jeong, Shinya Komugi, Françoise Combes, Martin Bureau, Lisa M. Young, Sukyoung K. Yi, and Roger L. Davies (2009). "Star formation and molecular gas in SAURON early-type galaxies". In: *Monthly Notices of the Royal Astronomical Society* 393.3, pp. 1255–1274. DOI: 10.1111/j.1365-2966.2008.14292.x.

D'Onghia, E., M. Vogelsberger, and L. Hernquist (2013). "Resonant Dynamics of Galactic Disks and Warps". In: *The Astrophysical Journal* 766, p. 34. DOI: 10.1088/0004-637X/766/1/34.

Davis, Timothy A., Katherine Alatalo, Marc Sarzi, Martin Bureau, Lisa M. Young, Leo Blitz, Paolo Serra, Alison F. Crocker, Davor Krajnović, Richard M. McDermid, Maxime Bois, Frédéric Bournaud, Michele Cappellari, Roger L. Davies, Pierre-Alain Duc, P. Tim de Zeeuw, Eric Emsellem, Sadegh Khochfar, Harald Kuntschner, Pierre-Yves Lablanche, Raffaella Morganti, Thorsten Naab, Tom Oosterloo, Nicholas Scott, and Anne-Marie Weijmans (2011). "The ATLAS^{3D} project – X. On the origin of the molecular and ionized gas in early-type galaxies". In: *Monthly Notices of the Royal Astronomical Society* 417.2, pp. 882–899. DOI: 10.1111/j.1365-2966.2011.19355.x.

E-MILES: Photometric predictions based on E-MILES SEDs (). Accessed: 2025-11-15. MILES website. URL: https://research.iac.es/proyecto/miles/pages/photometric-predictions-based-on-e-miles-seds.php.

Emsellem, Eric, Michele Cappellari, Davor Krajnović, Katherine Alatalo, Leo Blitz, Maxime Bois, Frédéric Bournaud, Martin Bureau, Roger L. Davies, Timothy A. Davis, P. Tim de Zeeuw, Sadegh Khochfar, Harald Kuntschner, Pierre-Yves Lablanche, Richard M. McDermid, Raffaella Morganti, Thorsten Naab, Tom Oosterloo, Marc Sarzi, Nicholas Scott, Paolo Serra, Anne-Marie Weijmans, and Lisa M. Young (2011). "The ATLAS^{3D} Project – III. A census of the stellar angular momentum within the effective radius of early-type galaxies: unveiling the distribution of fast and slow rotators". In: *Monthly Notices of the Royal Astronomical Society* 414.2, pp. 888–912. DOI: 10.1111/j.1365-2966.2011.18496.x.

Evans, N. W. and J. L. Collett (1994). "Counter-Rotating Cores in Elliptical Galaxies". In: *The Astrophysical Journal* 420, p. L67. DOI: 10.1086/187168.

Ferguson, Henry C. (1989). "Population Studies in Groups and Clusters of Galaxies. II. A Catalog of Galaxies in the Central 3.5 degrees of the Fornax Cluster". In: *The Astronomical Journal* 98. Used as reference for cluster distance (17 Mpc) in Morelli et al. (2017), p. 367.

Fisher, David (1994). "The dynamics and structure of the S0 galaxy NGC 7332". In: *The Astronomical Journal* 107.1, pp. 160–172. DOI: 10.1086/116841. URL: https://ui.adsabs.harvard.edu/abs/1994AJ....107..160F.

Freeman, K. C. (1970). "On the Disks of Spiral and S0 Galaxies". In: *The Astrophysical Journal* 160, pp. 811–830.

Galletta, G. (1987). "Detection of retrograde gas streaming in the SB0 galaxy NGC 4546". In: *The Astrophysical Journal* 318, pp. 531–535. DOI: 10.1086/165389. URL: https://ui.adsabs.harvard.edu/abs/1987ApJ...318..531G/abstract.

Garcia, A. M. (1993). "General study of group membership. II - Determination of nearby groups". In: *Astronomy and Astrophysics Supplement Series* 100, pp. 47–90.

Gasymov, Damir, Ivan Yu. Katkov, Evgenii V. Rubtsov, Anna S. Saburova, Alexei Yu. Kniazev, Joseph D. Gelfand, Olga K. Sil'chenko, Igor V. Chilingarian, Alexei V. Moiseev, Anastasia V. Kasparova, and Anatoly Zasov (Nov. 10, 2025). "Stellar CoRGI in MaNGA: Stellar Counterrotating Galaxies Identified in the MaNGA Survey". In: *arXiv e-prints*. arXiv: 2504.02925v2. URL: https://arxiv.org/abs/2504.02925v2.

Graham, Alister W. and Simon P. Driver (2005). "A concise reference to (projected) Sérsic $R^{1/n}$ quantities, including concentration, profile slopes, Petrosian indices and Kron magnitudes". In: *Publications of the Astronomical Society of Australia* 22.2, pp. 118–127. DOI: 10.1071/AS05001.

Hubble, Edwin (1936). *The Realm of the Nebulae*. New Haven: Yale University Press.

Katkov, I., I. Chilingarian, O. Sil'chenko, A. Zasov, and V. Afanasiev (2011). "A complex stellar line-of-sight velocity distribution in the lenticular galaxy NGC 524". In: *Baltic Astronomy* 20, pp. 453–458. DOI: 10.1515/astro-2017-0318. URL: https://ui.adsabs.harvard.edu/abs/2011BaltA..20..453K/abstract.

Katkov, I., O. K. Sil'chenko, and V. L. Afanasiev (2013). "Lenticular Galaxy IC 719: Current Building of the Counterrotating Large-Scale Stellar Disk". In: *Astrophysical Journal* 769.2, p. 105. DOI: 10.1088/0004-637X/769/2/105.

Khim, Donghyeon J., Sukyoung K. Yi, Yohan Dubois, Christophe Pichon, Julien Devriendt, and Hoseung Choi (2021). "Star–Gas Misalignment in Galaxies. II. Origins Found from the Horizon-AGN Simulation". In: *The Astrophysical Journal Supplement Series* 254.2, p. 27. DOI: 10.3847/1538-4365/abf1e0.

Kormendy, John and Ralf Bender (2009). "Structure and Formation of Elliptical and Spheroidal Galaxies". In: *The Astrophysical Journal Supplement Series* 182.1, pp. 216–309. DOI: 10.1088/0067-0049/182/1/216.

Krajnović, Davor, Eric Emsellem, Michele Cappellari, Katherine Alatalo, Leo Blitz, Maxime Bois, Frédéric Bournaud, Martin Bureau, Roger L. Davies, Timothy A. Davis, P. T. de Zeeuw, Sadegh Khochfar, Harald Kuntschner, Pierre-Yves Lablanche, Richard M. McDermid, Raffaella Morganti, Thorsten Naab, Tom Oosterloo, Marc Sarzi, Nicholas Scott, Paolo Serra, Anne-Marie Weijmans, and Lisa M. Young (2011). "The ATLAS^{3D} project – II. Morphologies, kinemetric features and alignment between photometric and kinematic axes of early-type galaxies". In: *Monthly Notices of the Royal Astronomical Society* 414.4, pp. 2923–2949. DOI: 10.1111/j.1365-2966.2011.18560.x.

Krajnović, Davor, Peter M. Weilbacher, Tanya Urrutia, Eric Emsellem, C. Marcella Carollo, Maryam Shirazi, Roland Bacon, Thierry Contini, Benoît Epinat, Sebastian Kamann, Thomas P. K. Martinsson, Matthias Steinmetz, and ... (2015). "Unveiling the counter-rotating nature of the kinematically distinct core in NGC 5813 with MUSE". In: *Monthly Notices of the Royal Astronomical Society* 452.1, pp. 2–18. DOI: 10.1093/mnras/stv958.

Kroupa, Pavel (2001). "On the variation of the initial mass function". In: *Monthly Notices of the Royal Astronomical Society* 322, pp. 231–246. DOI: 10.1046/j.1365-8711.2001.04022.x.

Kuijken, Konrad (1996). "The stellar velocity ellipsoid in disc galaxies". In: *The Astrophysical Journal* 471, pp. L1–L4. DOI: 10.1086/310332.

Lauberts, Andris and Edwin A. Valentijn (1989). *The Surface Photometry Catalogue of the ESO-Uppsala Galaxies*. Garching: European Southern Observatory.

Lovelace, R. V. E. and T. Chou (1996). "Magnetically driven warping and precession of accretion disks". In: *The Astrophysical Journal* 468, pp. L25–L28. DOI: 10.1086/310219.

Maraston, Claudia (2005). "Evolutionary population synthesis: models, analysis of the ingredients and application to high-z galaxies". In: *Monthly Notices of the Royal Astronomical Society* 362.3, pp. 799–825. DOI: 10.1111/j.1365-2966.2005.09270.x.

Michard, R. (1985). "Colors and luminosity distributions in elliptical galaxies". In: *Astronomy and Astrophysics* 59, pp. 205–217.

Morelli, L., E. M. Corsini, A. Pizzella, E. Dalla Bontà, L. Coccato, J. Méndez-Abreu, M. Cesetti, and F. Bertola (2015). "Stellar populations in counter-rotating components of galaxies". In: *Monthly Notices of the Royal Astronomical Society* 452.2, pp. 1128–1141. DOI: 10.1093/mnras/stv1356.

Morelli, L., A. Pizzella, L. Coccato, E. M. Corsini, E. Dalla Bontà, L. M. Buson, V. D. Ivanov, I. Pagotto, E. Pompei, and M. Rocco (2017). "Kinematic and stellar population properties of the counter-rotating components in the S0 galaxy NGC 1366". In: *Astronomy & Astrophysics* 600, A76. DOI: 10.1051/0004-6361/201630046.

Morelli, L., E. Pompei, A. Pizzella, J. Méndez-Abreu, E. M. Corsini, L. Coccato, R. P. Saglia, M. Sarzi, and F. Bertola (2008). "Stellar Populations of Bulges in 14 Cluster Disc Galaxies". In: *Monthly Notices of the Royal Astronomical Society* 389.1, pp. 341–357. DOI: 10.1111/j.1365-2966.2008.13569.x.

NASA/IPAC Extragalactic Database (2025). *NGC 1366 – Detailed information. By Name search result*. https://ned.ipac.caltech.edu/byname?objname=ngc+1366&hconst=67.8&omegam=0.308&omegav=0.692&wmap=4&corr_z=1. Accessed: 2025-08-21.

Pizzella, A., E. M. Corsini, J. C. Vega Beltrán, and F. Bertola (2004). "Ionized gas and stellar kinematics of seventeen nearby spiral galaxies". In: *Astronomy & Astrophysics* 424, pp. 447–453. DOI: 10.1051/0004-6361:20047104.

Pizzella, A., L. Morelli, E. M. Corsini, E. Dalla Bonta, M. Sarzi, and L. Coccato (2014). "Stellar kinematics and populations of spiral galaxy discs". In: *Astronomy & Astrophysics* 570, A79. DOI: 10.1051/0004-6361/201423769.

Posacki, Silvia (2014). "The dynamics of early-type galaxies as a tool to understand their hot coronae and their IMF". PhD thesis. Alma Mater Studiorum – Università di Bologna. URL: https://amsdottorato.unibo.it/id/eprint/15847/1/tesi.pdf.

Posacki, Silvia, Silvia Pellegrini, and Luca Ciotti (2013). "The effects of galaxy shape and rotation on the X-ray haloes of early-type galaxies". In: *Monthly Notices of the Royal Astronomical Society* 433.3, pp. 2259–2274. DOI: 10.1093/mnras/stt951. URL: https://academic.oup.com/mnras/article/433/3/2259/1229681.

Puerari, Ivân and Daniel Pfenniger (2001). "Gas Accretion and Counterrotation in Disk Galaxies". In: *The Astrophysical Journal* 558.2, pp. L43–L46. DOI: 10.1086/323484.

Renzini, Alvio and Alberto Buzzoni (1996). "Global Properties of Stellar Populations and the Spectral Evolution of Galaxies". In: *From Stars to Galaxies: the Impact of Stellar Physics on Galaxy Evolution*. Ed. by C. Leitherer, U. Fritze-von Alvensleben, and J. Huchra. Vol. 98. ASP Conference Series, pp. 195–231.

Ricciardelli, E., A. Vazdekis, A. J. Cenarro, and J. Falcón-Barroso (2012). "MIUSCAT: stellar population synthesis models with extended wavelength coverage". In: *Monthly Notices of the Royal Astronomical Society* 424.3, pp. 172–183. DOI: 10.1111/j.1365-2966.2012.21307.x.

Rubin, Vera C. (1994). "Multi-Spin Galaxies". In: *The Astronomical Journal* 108, pp. 456–464. DOI: 10.1086/117083. URL: https://ui.adsabs.harvard.edu/abs/1994AJ....108..456R/abstract.

Rubin, Vera C., J. A. Graham, and Jeffrey D. P. Kenney (1992). "Cospatial counterrotating stellar disks in the Virgo E7/S0 galaxy NGC 4550". In: *The Astrophysical Journal* 394,

pp. L9–L12. DOI: 10.1086/186460. URL: https://ui.adsabs.harvard.edu/abs/1992ApJ...394L...9R/abstract.

Sánchez-Blázquez, P., R. F. Peletier, J. Jiménez-Vicente, N. Cardiel, A. J. Cenarro, J. Falcón-Barroso, J. Gorgas, S. O. Selam, and A. Vazdekis (2006). "Medium-resolution Isaac Newton Telescope library of empirical spectra". In: *Monthly Notices of the Royal Astronomical Society* 371, pp. 703–718. DOI: 10.1111/j.1365-2966.2006.10722.x.

Sandage, Allan and John Bedke (1994). *The Carnegie Atlas of Galaxies*. Washington, DC: Carnegie Institution of Washington.

Satoh, Chū (1980). "Dynamical Models of Axisymmetric Galaxies and Their Application to the Elliptical Galaxy NGC 4697". In: *Publications of the Astronomical Society of Japan* 32, pp. 41–63.

Schombert, James M. (1986). "The structure of elliptical galaxies". In: *The Astrophysical Journal Supplement Series* 60, pp. 603–639. DOI: 10.1086/191100.

Sérsic, José Luis (1968). *Atlas de galaxias australes*. Córdoba, Argentina: Observatorio Astronómico, Universidad Nacional de Córdoba.

Silćhenko, Olga K., Alexei V. Moiseev, Alexandra A. Smirnova, and Roman I. Uklein (2023). "S0 Galaxies: Outer Gas Accretion through Tidal Interaction and Minor Merging". In: *Galaxies* 11.6, p. 119. DOI: 10.3390/galaxies11060119.

Thakar, A. R. and B. S. Ryden (1996). "Formation of Counterrotating Disks in Galaxies". In: *The Astrophysical Journal* 461, pp. 55–64. DOI: 10.1086/177041.

Thakar, A. R., B. S. Ryden, K. P. Jore, and A. H. Broeils (1997). "NGC 4138: A Case Study in Counterrotating Disk Formation". In: *The Astrophysical Journal* 479, pp. 702–719. DOI: 10.1086/303925.

Thomas, Daniel, Claudia Maraston, and Ralf Bender (2003). "Stellar population models of Lick indices with variable element abundance ratios". In: *Monthly Notices of the Royal Astronomical Society* 339.4, pp. 897–911. DOI: 10.1046/j.1365-8711.2003.06248.x.

Vaucouleurs, G. de (1948). "Recherches sur les Nebuleuses Extragalactiques". In: *Annales d'Astrophysique* 11, pp. 247–287.

Vaucouleurs, G. de, A. de Vaucouleurs, H. G. Corwin, R. J. Buta, G. Paturel, and P. Fouqué (1991). *Third Reference Catalogue of Bright Galaxies (RC3)*. Originally published by Springer-Verlag, with data also available via NASA/IPAC Extragalactic Database (NED). New York: Springer.

Vazdekis, A. (1996). "Spectral Energy Distributions for Old Stellar Populations. II. Near-Infrared Spectral Indices". In: *The Astrophysical Journal Supplement Series* 106, pp. 307–329. DOI: 10.1086/192338.

Vazdekis, A., M. Koleva, E. Ricciardelli, J. Falcón-Barroso, A. J. Cenarro, N. Cardiel, I. Pérez, and J. Gorgas (2016). "Evolutionary stellar population synthesis with the extended MILES spectral coverage". In: *Monthly Notices of the Royal Astronomical Society* 463.4, pp. 3409–3436. DOI: 10.1093/mnras/stw2212.

Vazdekis, A., E. Ricciardelli, A. J. Cenarro, J. Rivera-González, L. A. Díaz-García, and J. Falcon-Barroso (2012). "MIUSCAT: Extended MILES spectral coverage - I. Stellar population synthesis models". In: *Monthly Notices of the Royal Astronomical Society* 424.2, pp. 157–171. DOI: 10.1111/j.1365-2966.2012.21179.x.